

GLOBAL AND REGIONAL DATA ABOUT THE MOON

Paul Spudis and Carlé Pieters

Despite the major achievements in studying the Moon during the last quarter-century, our global knowledge is still patchy and incomplete. Although the Moon is so close, access has always been limited. Half of the Moon remained completely unknown until spacecraft could be sent around it. Even with the Apollo program and the Soviet and U.S. robotic lunar explorations, humans have directly explored only 6 sites on the Moon and soft-landed robots at another 10 (not counting the Surveyor 3 site, which was also visited by the Apollo 12 mission; see Table 2.1 and Figs. 2.1 and 2.2). These sites are all on the lunar nearside, and most of them are near the lunar equator. Sample return missions (both human and robotic) have provided information on only nine sites; even with the addition of Antarctic lunar meteorites (whose exact sources are unknown), the lunar sampling grid is still minimal.

To compensate for limited access, lunar scientists have two advantages. One advantage is technical. The instruments used for lunar exploration by both humans and robots, and the techniques used to analyze lunar samples back on Earth, were the most powerful and modern that could be applied. As a result, we have learned things about the Moon in a few years that took decades to learn about the Earth. A second advantage is the nature of the Moon itself. Compared to the Earth, the Moon is a simple world; it lacks the complications produced by plate tectonics, active volcanism, weather, water, and life. The geological history of the Moon, although complex and exciting, is potentially quite decipherable because it is simpler than Earth's. This is why

it has been possible, with only a few landings and sample returns, to establish the outlines of the Moon's origin and development and to identify the new scientific questions to be answered by future missions.

The next step in lunar studies is to acquire complete global information. It is paradoxical that the Apollo program, which provided so much information about a few parts of the Moon, did not also produce full global data about such key lunar characteristics as surface chemistry, surface mineral composition, gravity, magnetic fields, and topography—in short, a scientific database for the whole Moon as a single world.

The need for more global lunar data is clear, and so is the method necessary to collect it—a polar-orbiting spacecraft, equipped with an array of scientific instruments and able to scan the entire Moon over the course of a year. Proposed at various times under various names, the mission is now being actively studied as the Lunar Observer (see section 11.4.6), and is regarded as a key step in the further exploration of the Moon by both robots and human beings.

10.1. GLOBAL AND REGIONAL IMAGERY AND DATA SOURCES

Limited global and regional data for the Moon have so far been obtained primarily from three sources: telescopic observations of the Moon's nearside with Earth-based telescopes; photographs provided in the 1960s by a variety of unmanned

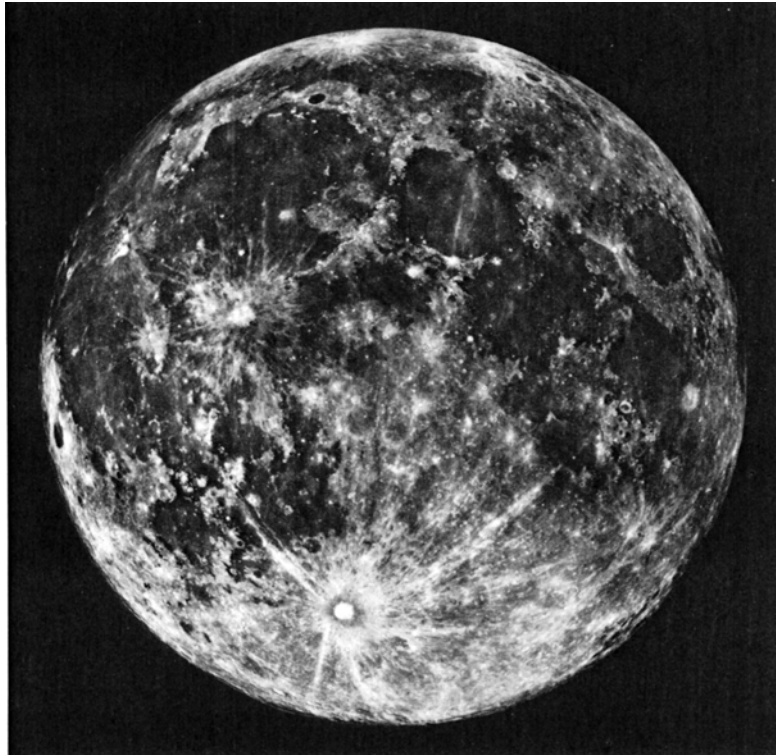


Fig. 10.1. Full-Moon photograph of the lunar nearside, obtained with the 36-in (91-cm) telescope at Lick Observatory, Mt. Hamilton, California. Lunar north is at top. The large, bright-rayed crater at the bottom (south) is Tycho. (Lick Observatory Catalog, Photo #L4. Reproduced by permission.)

missions, including the U.S. Ranger and Lunar Orbiter series, the U.S.S.R. Zond, and others; and measurements using instruments carried in lunar orbit on several Apollo command modules and in subsatellites released during several Apollo missions (1968–1972). Although none of these techniques has provided complete coverage of the entire surface of the Moon, they have provided preliminary information about the lunar magnetic and gravitational fields, the range of different lunar surface materials, and limited information on their distribution. Collections of the photographic images returned by the Lunar Orbiter and Apollo missions are available for examination at the NASA Planetary Data Centers (see front matter of this book).

10.1.1. Earth-based Telescopic Data

Since the first use of telescopes in the 17th century, increasingly larger and more sophisticated instruments have been pointed at the Moon by astronomers wanting to better understand the Earth's nearest neighbor. Current Earth-based observations of the Moon are limited not by telescope design and size, but by atmospheric conditions (weather, atmospheric absorptions, and general atmospheric stability) and by the availability

of appropriate instruments and detectors. Most measurements of moonlight are made through the atmospheric "window" of low absorption between 0.3 μm and 2.5 μm ; almost all the radiation that comes from the Moon in these wavelengths is reflected solar radiation.

Under ideal conditions, the best spatial resolution of lunar features observable from Earth is about 0.5 km near the center of the lunar disk, even for the largest ground-based telescopes. The full Moon photographic image shown in Fig. 10.1 is a good example of the imaging capabilities of Earth-based telescopes. For telescopes in low-Earth orbit above the atmosphere, spatial resolution should easily be about a factor of 10 better than for an equivalent telescope on the ground, and the light reflected from the Moon is not subject to atmospheric absorptions at various wavelengths. However, Earth-based or Earth-orbiting telescopes only allow observation of the nearside of the Moon, the side that always faces the Earth, and even the earliest unmanned missions in the 1960s showed clearly that the nearside is not representative of the whole Moon.

Despite the limited data available from Earth-based observations, the Earth-based vantage point has a number of advantages in convenience that result from the closeness and the ready accessibility

of the Moon. From Earth, individual areas on the Moon can be observed repeatedly under a variety of lighting conditions, allowing small-scale surface features (which cannot be captured in a single photograph) to be identified and studied. Such Earth-based observations were used extensively in the early (pre-Apollo) geological mapping program of the Moon. Furthermore, as technology progresses and new sensing instruments are developed, they can be deployed immediately on existing telescopes to collect new or additional data (see section 10.2.1). Finally, the Moon has been observed by Earth's inhabitants for thousands of years, although at relatively low resolution (about 100 km for a good pair of eyes). Although the Moon appears to have been an inactive planet for much longer than this, one possible large meteoroid impact event on the Moon may have been optically observed and recorded in historic time, about 800 years ago (e.g., *Hartung*, 1976).

10.1.2. Lunar Orbiter Photographic Images

The five Lunar Orbiter spacecraft, placed in lunar orbit in 1966–1967, were designed to carry out three basic activities: (1) photography to obtain both detailed, high-resolution photographs needed for the future Apollo landings and pictures of general scientific interest; (2) geodesy to accurately map the lunar gravitational field; and (3) measurements of the lunar radiation and micrometeoroid environment. The five Lunar Orbiter spacecraft were all successful; they returned 1654 photographs, of which about half were taken near the lunar equator for Apollo site selection purposes. Because the first three Lunar Orbiters obtained all the imagery required for the Apollo site selection, the last two missions, Lunar Orbiters 4 and 5, were placed in polar orbits to systematically map the entire Moon and to photograph regions of high scientific interest.

The Lunar Orbiter cameras recorded two frames simultaneously on film: a wide-angle view (80-mm lens) and a narrow-angle view (160-mm lens). The film was developed onboard the spacecraft in lunar orbit. The resulting images were then optically scanned by a video system and radioed to Earth. This analog (not digital) video signal was then used to expose similar film on Earth. The process was similar to the operation of a conventional FAX or wirephoto machine. The final complete Lunar Orbiter dataset consists of hard-copy, black-and-white photographs assembled from strips (for details, see *Hansen*, 1970).

The data returned by Lunar Orbiter 4 in particular provided nearly complete coverage of the lunar nearside at about 100 m resolution. These photo-

graphs (see Fig. 10.2 and section 10.6 on Apollo landing sites) remain the single most useful collection of photographs of the lunar nearside. A series of high-resolution images provided by Lunar Orbiter 5 and covering small-area scientific targets (e.g., volcanoes within the rings of Mare Orientale) have been used in many subsequent detailed studies (e.g., *Wilhelms*, 1987).

Documents providing compilations and overview of the Lunar Orbiter dataset include an atlas of the entire Moon, based on Lunar Orbiter photographs (*Bowker and Hughes*, 1971), a nearside-only compilation including surface-feature nomenclature (*Gutschewski et al.*, 1971), an excellent user's guide and index to the data collection (*Hansen*, 1970), and useful introductions to both Lunar Orbiter photographs and the general geology of the Moon (*Kosofsky and El-Baz*, 1970; *Schultz*, 1976a).

10.1.3. Apollo Orbital Photography

All the Apollo missions to the Moon, even the ones that did not land, carried out lunar photography, both from lunar approach and in lunar orbit. During the first five lunar missions (Apollo 8 and 10–13), the astronauts took numerous photographs from the command module using a 70-mm Hasselblad handheld camera and a Maurer 16-mm movie camera. In addition, the Apollo 14 mission carried an automated high-resolution mapping camera that unfortunately failed after a few orbits.

In addition to the astronaut-operated cameras in the command module, the last three Apollo missions (Apollo 15–17) carried two automatic cameras in the attached service module. The first, a mapping (metric) camera, was designed to produce moderate-resolution (50 m), cartographic-quality stereo images of the surface along the spacecraft groundtracks (Fig. 10.3). The second was an optical-bar, panoramic camera whose pictures included the surface immediately below the spacecraft at very high resolution (1–2 m) and then included “wings” of progressively lower-resolution imagery out to 54° to each side, perpendicular to the ground track. The photographs produced by these two cameras are of excellent quality, but the coverage is unfortunately limited to the near-equatorial regions overflown by the Apollo 15–17 missions. A series of high-quality topographic maps at 1:250,000 scale (the Lunar Topographic Orthophotomap series) was prepared from the Apollo metric photography by the Defense Mapping Agency (DMA).

Masursky et al. (1978) provide an excellent introduction to the Apollo orbital photography dataset. This superbly illustrated book describes the Apollo photographic systems and gives numerous

Fig. 10.2. Lunar Orbiter 4 photograph showing the typical quality of the high-resolution Lunar Orbiter frames (resolution 100 m), which cover most of the lunar nearside. The area shown is near the southwestern border of Mare Serenitatis. Lunar north is at the top. The photograph shows the boundary between relatively smooth (dark) mare material (upper) and more rugged highlands (lower). The prominent crater is Sulpicius Gallus (12 km diameter). Low-albedo materials in the highlands consist of dark-mantle pyroclastic deposits. The original negatives were developed in the spacecraft and read by a photomultiplier in strips for transmission to Earth; these strips are called "framelets," and the boundaries between framelets cause the horizontal lines seen in this figure. Each framelet shows a strip of lunar surface 11 km wide. The white blemish at the left side is a flaw in the film developed in the spacecraft. (Portion of NASA Photo LOIV-97H.)

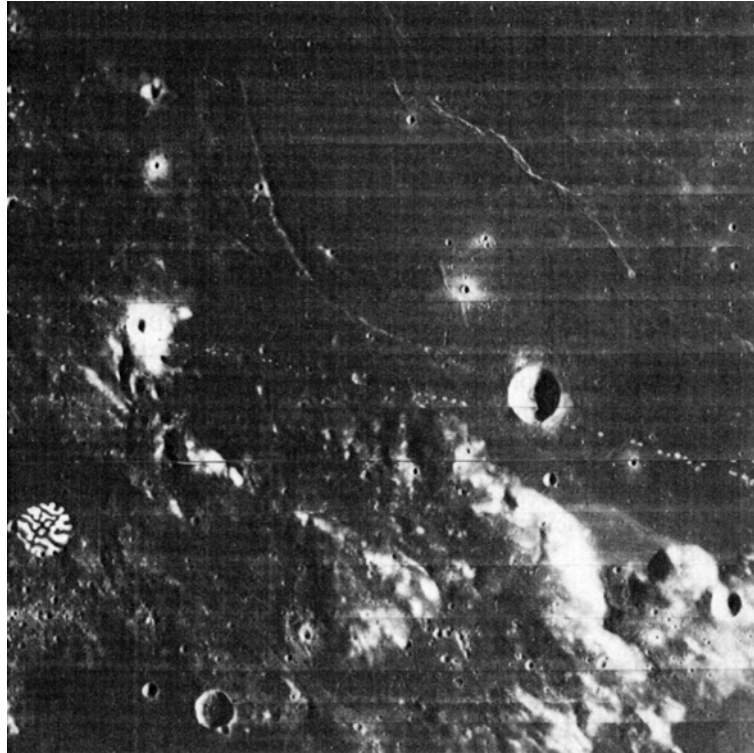
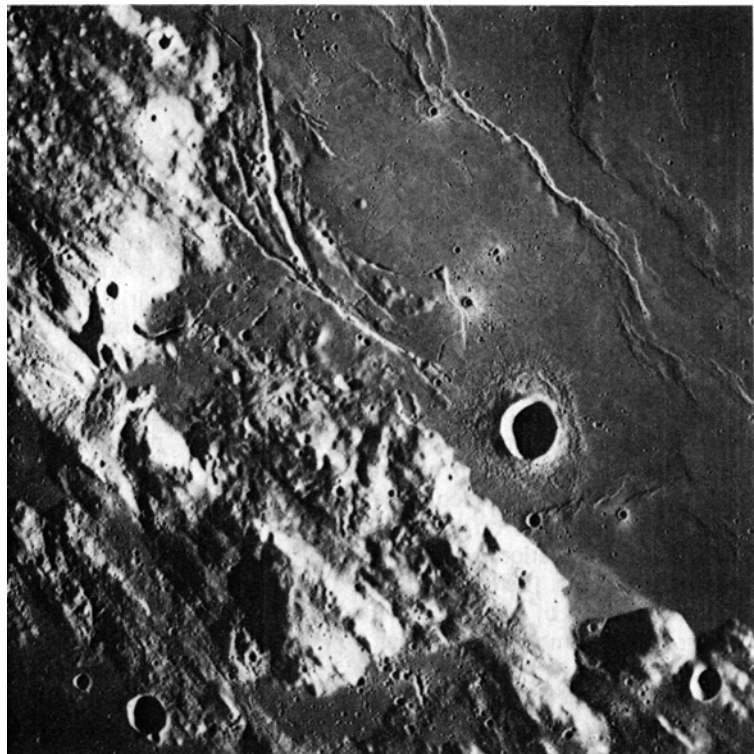


Fig. 10.3. Apollo 17 mapping (metric) camera view of the Sulpicius Gallus region along the southwestern border of Mare Serenitatis. Lunar north is at the top. This figure shows the same boundary region between mare material (upper right) and highlands (lower left) that is shown in Fig. 10.2. This photograph illustrates the general quality of these mapping camera pictures in comparison to Lunar Orbiter imagery (Fig. 10.2). The mapping camera pictures have higher ground resolution (about 50 m) and were taken at lower-angle solar illumination, thus enhancing surface details. Adjacent mapping camera frames have about 30% overlap, permitting stereo viewing. (Apollo 17 Metric Frame 1514.)



examples and geologic interpretations of lunar features using a variety of Apollo photographs. A series of Apollo flight photo indexes and all of the lunar topographic maps prepared from Apollo photographs are obtainable from the National Space Science Data Center (NSSDC) at the NASA/Goddard Space Flight Center in Greenbelt, Maryland; see *Cameron et al.* (1977) for details.

10.1.4. Coverage and Resolution of Lunar Photography

Although virtually the entire lunar surface has been photographed from orbit, the wide variety of missions and photographic systems used in lunar exploration has resulted in an uneven coverage of the Moon in terms of both resolution and image quality (lighting conditions). Virtually all lunar image data is in nondigital (hard copy) form. These image data therefore cannot be digitally processed to enhance contrast and surface detail, nor can they be manipulated to coordinate with other data obtained from the same region. A map showing the variety of resolutions of available lunar surface photographic coverage is given in Fig. 10.4. This map summarizes all available lunar photography from Ranger through Apollo. More detailed discussions of current photographic coverage of the Moon are found in *Heinzen and Peer* (1971) and in the Lunar Geoscience Observer Workshop Report (*LGO Science Workshop Members*, 1986).

10.2. SURFACE MINERALOGIC AND GEOCHEMICAL DATA

Three remote-sensing techniques, involving visible, near-infrared (IR), gamma-ray, and X-ray radiation, have been used successfully to measure the composition of the Moon in selected regions. Spectral measurements of reflected visible and near-IR radiation continue to provide information about the mineralogy of the lunar surface material. All currently available visible and near-IR reflectance data have been acquired using Earth-based telescopes (sections 6.2.1, 6.5, and 7.2). The elemental abundances at the lunar surface have been measured from lunar orbit for Th, U, K, Fe, and Ti using gamma-ray spectrometers, and for Mg, Si, and Al using X-ray spectrometers; both instruments were carried in the Apollo 15 and 16 orbiting spacecraft.

10.2.1. Spectral Reflectance Measurements and Multispectral Imagery (Earth-based)

Even to the naked eye, the surface of the Moon exhibits distinct differences in brightness associated with different geological units; the basaltic maria are dark and the feldspathic highlands are bright (see

discussion of optical astronomy in section 9.3.1). Differences in the relative “redness” or “blueness” between different surface units on the Moon have also been known since the early part of this century (*Wood*, 1912).

The spectral character of radiation reflected from the Moon is controlled largely by the mineralogic composition of the lunar surface. When measured at high spectral resolution (<1%) the reflected solar radiation in the visible and near-IR wavelengths exhibits absorption features that are diagnostic of surface mineralogy (e.g., *Adams*, 1974, 1975; *McCord and Adams*, 1973; see sections 6.2.1, 6.5, and 7.2 for detailed discussions of the spectral characteristics of lunar materials measured in the laboratory). Although mineral composition is the primary factor controlling the spectral character of lunar surface materials, differences in physical properties (e.g., particle size, compaction) and in the results of exposure to the lunar environment (micrometeoroid impact products: glass, agglutinates, etc.) affect both the overall brightness and the relative strengths of individual spectral absorptions.

Reflectance spectra measured on the Moon from Earth-based telescopes currently exist for a few hundred individual areas 5–20 km in diameter for the spectral range 0.3–1.1 μm (e.g., *McCord et al.*, 1972a,b; *Pieters and McCord*, 1976; *Pieters*, 1977). Near-infrared (0.6 to 2.5 μm) spectrometers, capable of producing precise spectra of high spectral resolution, were developed in the mid-1970s, thus making possible telescopic measurements of lunar areas only 3.7 km in diameter (*McCord et al.*, 1981). At these resolutions, compositional variations across relatively small lunar features (e.g., individual craters in the 50- to 100-km-diameter range) can be studied in detail. Detailed remote analysis of the mineral composition of the lunar surface material then became possible with these spectra, and the new compositional information was applied to a variety of important lunar science problems (*Pieters et al.*, 1980, 1983, 1985; *Bell and Hawke*, 1981, 1984; *Hawke and Bell*, 1981; *Pieters*, 1982; *Spudis et al.*, 1984; *Gaddis et al.*, 1985; *Lucey et al.*, 1986; *Smrekar and Pieters*, 1985). Summaries of available spectral reflectance data for the lunar nearside, including both maria and highland crustal regions, can be found in *Pieters* (1978) and *Pieters* (1986), respectively.

Until similar spectroscopic measurements are made from a lunar-orbiting spacecraft, no global spectral data will exist for the Moon, especially for the lunar farside. In the meantime, the information obtained from the slowly increasing number of Earth-based high-resolution spectra obtained for individual small lunar areas are providing a good

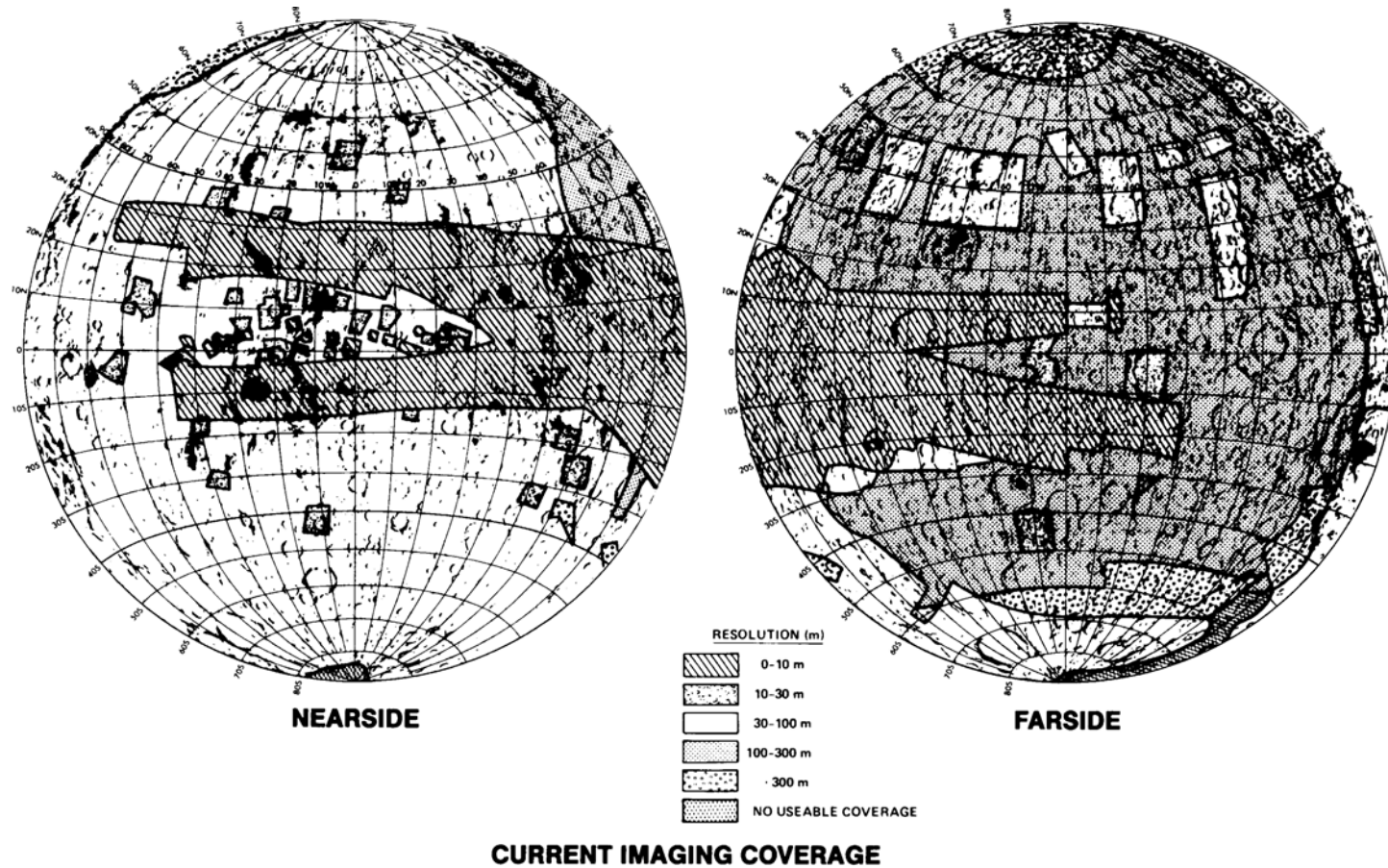


Fig. 10.4. Nearside and farside maps of the Moon showing photographic coverage of the lunar surface from all missions in terms of ground resolution. The best coverage (0–10 m resolution) is in the equatorial “Apollo zone” (east limb, 30°N to 20°S), where the candidate Apollo landing sites were located. However, even in this intensely-covered region, many photographs from longitude 70°E to 100°E were taken under nearly vertical solar illumination, making them less desirable for studying lunar surface features. Data from *Heinzen and Peer* (1971) and the Lunar Cartographic Dossier (*Schirmerman*, 1973).

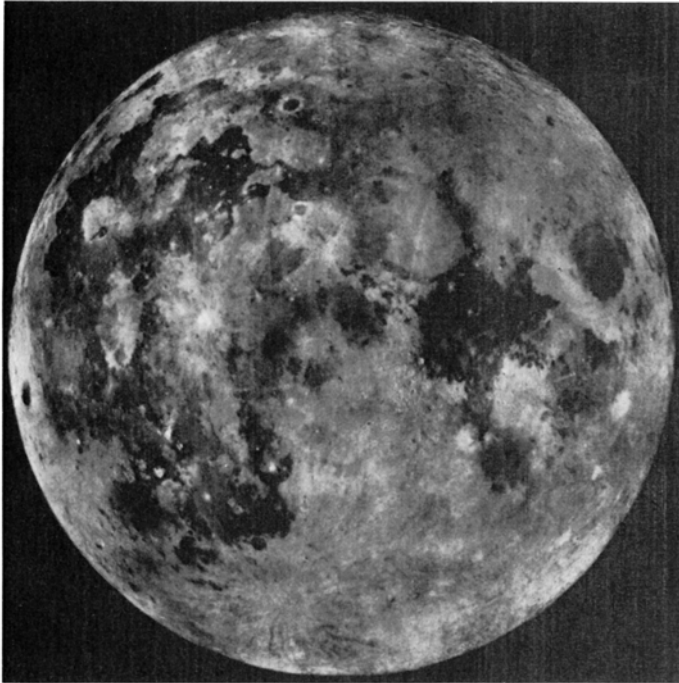


Fig. 10.5. Color-difference photograph of the lunar nearside, obtained in 1973 with the 61-in (155-cm) Catalina (Arizona) reflector (E. Whitaker, personal communication, 1980). Lunar north is at the top. This photograph is a composite image mosaic produced from carefully controlled individual photographs taken at wavelengths of $0.38\ \mu\text{m}$ (negatives) and $0.62\ \mu\text{m}$ (positives). In this figure, relatively blue surface regions appear dark, and relatively red regions appear bright. These color differences are particularly sensitive to the Ti content of lunar mare soils; Ti-rich soils appear bluish and are therefore dark in this image.

characterization of the surprisingly large variety of rock types that are present across the lunar nearside (see discussion in section 10.4.3). It is already clear, for example, that the range of lunar rock types is much greater than represented by the samples returned from the nine Apollo and Luna sites or collected as meteorites in Antarctica.

The spatial extent of spectral variations across the lunar surface is often examined using *multispectral images*, in which surface-image data are gathered for a few selected spectral channels. If the channels chosen are those in which lunar materials exhibit significant spectral contrast, then surface color variations (and hence surface compositional variations) can be mapped using two-dimensional detectors. Although multispectral images do not normally provide the high-spectral-resolution data required to identify individual mineral species, the images are well-suited for efficiently defining the spatial extent of a particular surface unit. Figure 10.5 shows a full-Moon color difference mosaic prepared from composite photographic images taken at $0.38\ \mu\text{m}$ (negative) and $0.62\ \mu\text{m}$ (positive) (E. Whitaker, personal communication, 1980; see Whitaker, 1972 for a discussion of the technique). In this composite image, surface units that have a high $0.38\text{-}\mu\text{m}/0.62\text{-}\mu\text{m}$ reflectance ratio appear dark, and units with a low ratio appear bright. This ratio is

sensitive to the Ti abundance of lunar mare soils (e.g., Charette *et al.*, 1974; Pieters, 1978) and is thus particularly useful for identifying the spatial extent of different basaltic surface units having different Ti contents, e.g., the high-Ti basalts at the Apollo 11 and 17 sites and the low-Ti basalts at the Apollo 12 and 15 sites (see also Plate 10.7 and discussion in section 10.4.1).

High-resolution ($\sim 2\ \text{km}$) digital multispectral images of selected lunar regions were obtained with Earth-based telescopes in the 1970s using vidicon imaging systems (e.g., McCord *et al.*, 1976, 1979; Johnson *et al.*, 1977). Because these images were virtually the only high-precision digital images available during the 1970s and 1980s, they have been extensively used in numerous scientific studies of specific areas on the Moon. The full set of these vidicon images has also provided some of the principal data used to define lunar basalt types on the nearside of the Moon (section 10.4.1). The example shown in Fig. 10.6 is a single set of three visible/near-IR vidicon frames, centered on the Apollo 12 landing site in Oceanus Procellarum (Pieters and McCord, 1976). These images were obtained using filters with bandwidths of $\sim 30\ \text{nm}$ and centered at 0.40 , 0.56 , and $0.95\ \mu\text{m}$. These wavelengths were chosen to be particularly sensitive to (1) the relative brightness of surface features

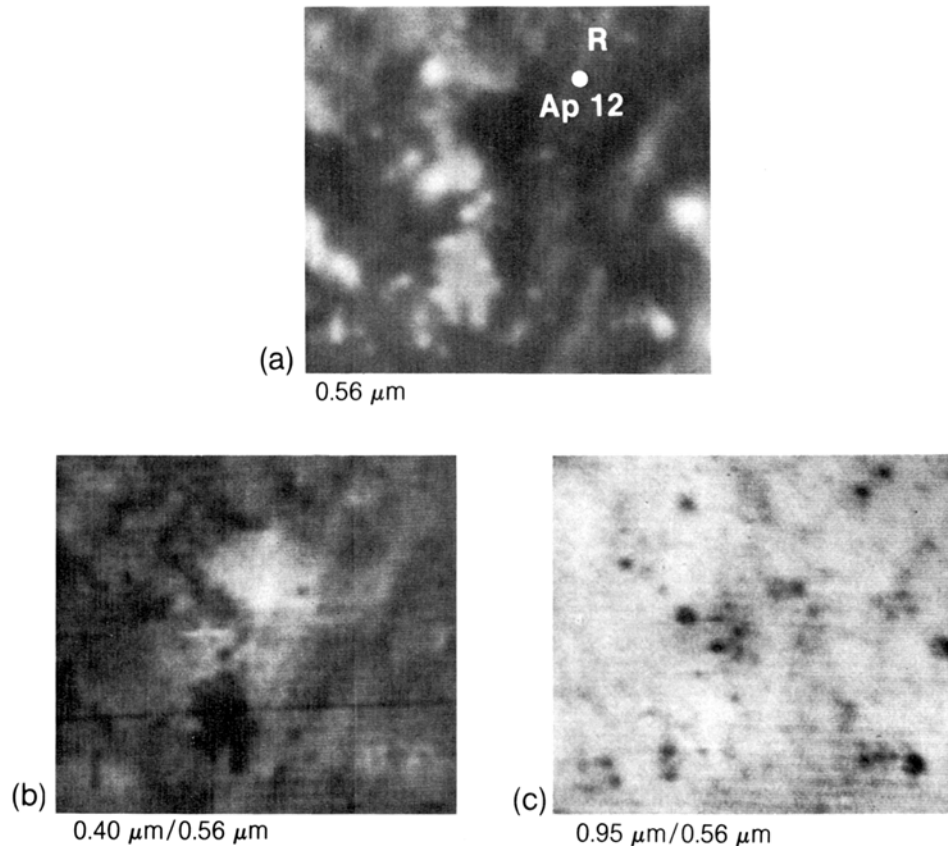


Fig. 10.6. Multispectral images of the Apollo 12 landing site in Oceanus Procellarum, obtained with a vidicon imaging system using Earth-based telescopes. Lunar north is at the top. The 0.56- μm image **(a)** (slightly enhanced) shows prominent albedo variations across the site. Low-albedo surfaces are basaltic mare lavas. Small craters superimposed on the mare and nearby highlands appear bright because they expose fresh material. A crater ray ("R"; thought to be from Copernicus) extends from north to south-southwest across the landing site ("Ap 12"). The two color ratio images **(b,c)** provide different information about surface composition. The 0.40- μm /0.56- μm image **(b)** includes wavelengths that are sensitive to Ti content, and has been enhanced to display the compositional variations of the basaltic surface in this region. A relatively large basalt area (bright area in center), with higher Ti content than most lavas in the Apollo 12 region, occurs to the southwest of the Apollo 12 site. The 0.95- μm /0.56- μm image **(c)** is sensitive to the strength of a mafic mineral absorption band near 1.0 μm . Low values (dark areas in the image) indicate strong absorption and correspondingly high contents of mafic minerals, mostly pyroxene. The freshly-exposed surface material around young craters generally contains a higher component of crystalline material, and these areas therefore exhibit stronger absorptions caused by mafic minerals. Field of view is ~ 150 km.

(0.56 μm), (2) spatial variations in different basaltic surface units (0.40 μm /0.56 μm), and (3) spatial variations of the strength of mafic mineral absorption bands (0.95 μm /0.56 μm).

10.2.2. Apollo Gamma-ray Spectrometer

Both the Apollo 15 and 16 service modules carried a gamma-ray spectrometer with a NaI(Tl) crystal detector. This instrument was capable of measuring

lunar surface gamma-ray radiation and identifying discrete lines in the energy spectrum that were characteristic of individual elements. Two types of lines were observed as signals in the measured spectrum. The first group is caused by natural lunar radioactivity and is produced by the decay of lunar ^{40}K , ^{238}U , and ^{232}Th . The second group of lines results from the bombardment of the Moon by high-energy galactic-cosmic-ray (GCR) particles. This bombardment produces secondary particles (mostly neutrons)

within the lunar surface materials and also excites the nuclei of certain elements. This excitation produces characteristic gamma-ray lines for the elements Fe, Ti, Al, and Si (see discussion in *Arnold et al.*, 1972).

Data from the gamma-ray spectrometers onboard the Apollo 15 and 16 spacecraft have been processed into elemental abundance maps for Th (*Metzger et al.*, 1977; Plate 10.1), Fe (*Davis*, 1980; Plate 10.2), and Ti (*Metzger and Parker*, 1979; *Davis*, 1980; Plate 10.3). The orbital Th data are the most precise (*Metzger et al.*, 1977). The abundance maps for Fe and Ti are derived by a complex iterative process that includes examining the spectra for the expected lines from these elements and then extracting actual concentration levels by comparing the “ground-truth” chemical data derived from laboratory analyses of returned regolith samples from Apollo and Luna landing sites with the gamma-ray spectra measured while flying over those same sites.

The precision of orbital gamma-ray elemental data is dependent on the time spent counting a given area; more counting time results in better statistical precision. Because the time spent in lunar orbit during the Apollo missions was limited, the precision of these orbital data is fairly low (10–25% relative for Fe; 30–50% relative for Ti). The surface or ground resolution of the data is a function of spacecraft altitude, and about 100 km is the nominal resolution of the Apollo gamma-ray data. Detailed discussion of data reduction can be found in *Bielefeld et al.* (1976). Discussions of error analysis and the derivation of Th, Fe, and Ti concentrations are found in *Metzger et al.* (1977), *Metzger and Parker* (1979), and *Davis* (1980), respectively. *Davis and Spudis* (1987) provide error magnitude maps for the Th, Ti, and Fe measurements.

10.2.3. Apollo X-ray Fluorescence Spectrometer

Because the Moon has no absorbing atmosphere, solar radiation at all wavelengths reaches the lunar surface. The Apollo 15 and 16 orbital spacecraft carried X-ray fluorescence spectrometers to measure the fluorescent X-rays produced by the excitation of atoms in the lunar surface by the incident solar X-rays. Measurement of the X-rays given off from the Moon can be used to determine the concentration of elements of atomic number 14 (Si) or less in lunar surface materials. Because no absolute calibration of the incident solar X-ray flux was included on the Apollo spacecraft, the experimental data could only be expressed as ratios of Al/Si and Mg/Si. Surface maps of these ratios were produced along the Apollo 15 and 16 groundtracks

across the hemisphere of the Moon that was sunlit (and therefore exposed to solar X-rays) during these missions (Plates 10.4 and 10.5). The effective ground resolution of the Apollo X-ray data is much greater than that of the gamma-ray data; the nominal surface resolution is about 30 km (*Andre et al.*, 1977).

The Apollo orbital X-ray data provide information on the distribution of the geochemically significant elements Mg and Al, and they have therefore been used in numerous studies relating to the global magmatic history of the Moon (e.g., *Adler et al.*, 1973; *Hubbard*, 1979). Unfortunately, such X-ray data can only be collected from sunlit regions of the Moon; as a result of the relatively short Apollo missions, this information is available for only about 9% of the lunar surface. For details on the Apollo X-ray orbital chemical data, see *Adler et al.* (1972), *Adler and Trombka* (1977), *Clark and Adler* (1978), and *Clark and Hawke* (1981).

10.3. GEOPHYSICAL DATA

Several types of lunar geophysical data have been acquired by lunar-orbiting spacecraft and from Earth-based observations. This section summarizes information on the lunar gravity field, the surface magnetic field, and the radar-backscatter properties of the lunar surface.

10.3.1. Lunar Gravity Field

Current knowledge of the Moon’s gravitational field has come principally from radio-tracking data provided by orbiting lunar spacecraft. These investigations involve measuring the Doppler shift of the spacecraft’s transmitted radio signal as it flies over various lunar features. As the spacecraft’s orbital path is perturbed by lunar mass excesses or deficiencies beneath it, its orbital velocity (and hence the Doppler shift of its signal) changes. These changes can then be used to understand the structure of the lunar gravity field. Because direct spacecraft-to-Earth transmissions have been used with the single-spacecraft missions so far, only gravity data for the lunar nearside are available.

The gravity data obtained from the polar-orbiting Lunar Orbiter 4 and 5 missions (Fig. 10.7) resulted in the discovery of lunar *mascons* (i.e., mass concentrations; *Müller and Sjogren*, 1968, 1969). These mascons are large, positive gravity anomalies associated with some basalt-filled lunar basins. These gravity anomalies still have not been satisfactorily explained. Hypotheses of origin range from the relatively high density of the mare basalts filling the basins (*Phillips et al.*, 1972), to the presence of

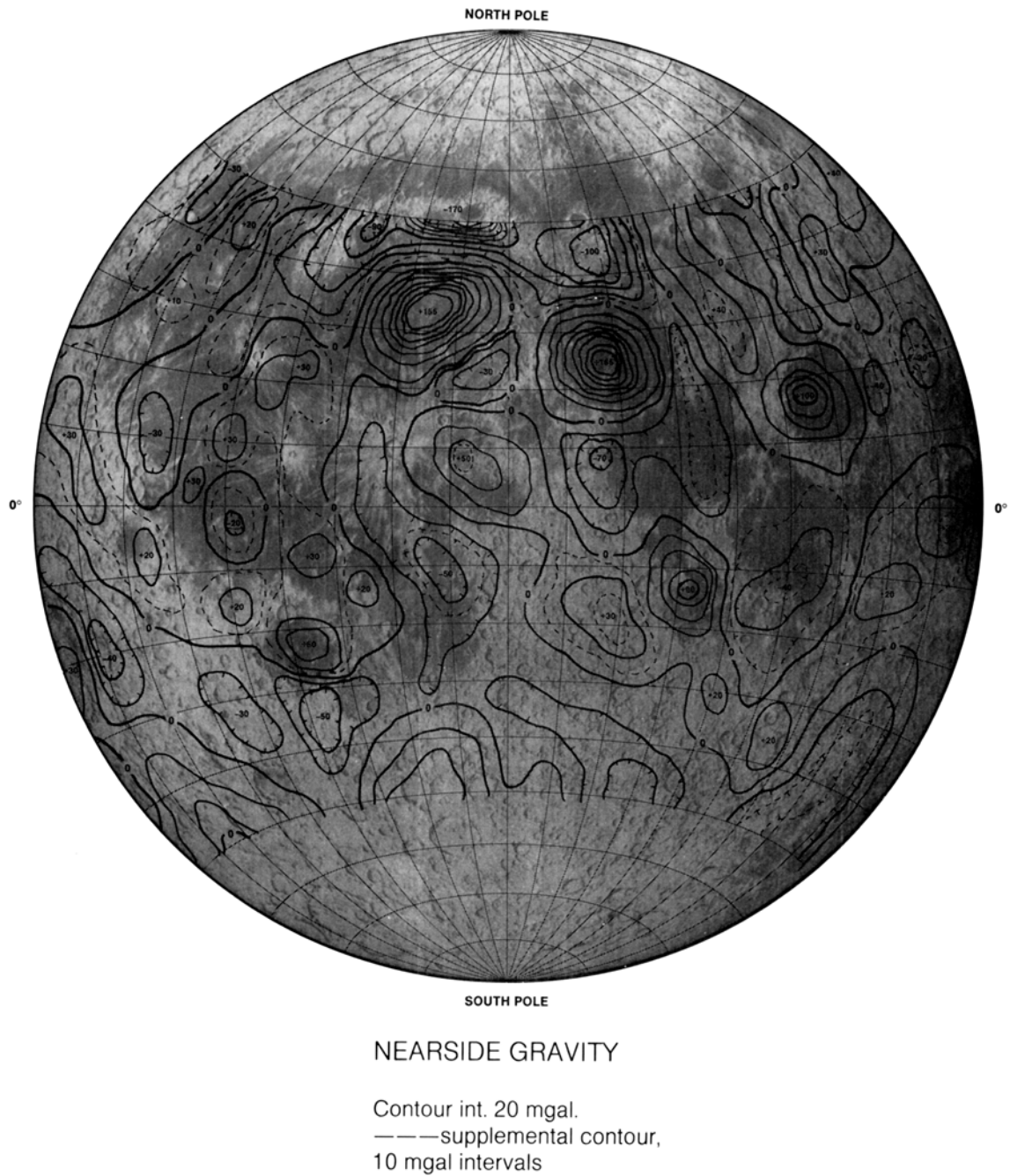


Fig. 10.7. Map of lunar nearside gravity field derived from radio tracking of the Lunar Orbiter 3, 4, and 5 spacecraft (Müller and Sjogren, 1968, 1969). Lunar north is at top. Contour interval is 20 milligals (mgal); supplemental 10-mgal contours (dashed lines) are shown for low-contrast regions. Closed contours around positive values indicate concentrations of excess mass (*mascons*), many of which are associated with the lunar maria. The largest mascon (+165 mgal) is associated with Mare Serenitatis; the second largest (+155 mgal) is associated with Mare Imbrium.

uplifted mantle material (Wise and Yates, 1970), to some combination of the two (Bowin *et al.*, 1975; Phillips and Dvorak, 1981).

10.3.2. Lunar Surface Magnetic Field

It was recognized early in lunar exploration that the Moon possesses at most a very weak internal magnetic field, and it is not yet clear that one exists at all. Surface magnetic measurements were performed by the surface magnetometers deployed at fixed locations at the Apollo 12, 15, and 16 sites. On the Apollo 14 and 16 missions, the astronauts used portable magnetometers to measure the magnetic fields along traverses within the landing area (Dyal *et al.*, 1974). These surface measurements found anomalous local areas with remanent magnetic fields as strong as 300 γ , or 0.24 A/m (a field strength that is still two orders of magnitude less than Earth's; see Table 3.1). Two subsatellites launched into lunar orbit from the Apollo 15 and 16 service modules carried magnetometers (Coleman *et al.*, 1972) to measure surface magnetism directly. These subsatellites also carried electron detectors that could indirectly determine smaller-scale surface magnetic fields by measuring the fluxes of electrons reflected from the lunar surface by magnetic anomalies (Lin *et al.*, 1976; Plate 10.6). The maximum signal detected at the subsatellite was about 0.0080 A/m ($\sim 10 \gamma$), with a sensitivity of 0.0002 A/m (0.2 γ).

The measurements of reflected electrons by the subsatellites (Lin *et al.*, 1976) indicate that about 5% of the lunar maria surfaces have a significant magnetic field (i.e., detected by the subsatellites as a signal >0.0004 A/m, or $>0.4 \gamma$). These measurements also demonstrate that, in general, the lunar maria show relatively weak, bland surface fields, whereas the highlands display a diverse and heterogeneous field strength distribution. For reviews of the interpretations of lunar magnetic data, see Fuller (1974), Dyal *et al.* (1974), and Hood *et al.* (1979).

A major unresolved problem concerning lunar surface magnetism is the existence of localized strong magnetic anomalies detected from orbit (Plate 10.6), including those in the Reiner Gamma region (nearside) and near Van de Graaff Crater (farside). Several of these anomalies occur on the opposite sides of the Moon (antipodal) from young mare impact basins such as Imbrium and Crisium (Hood, 1987). The anomalies are often associated, especially at Reiner Gamma, with a peculiar pattern of light- and dark-colored swirls on the lunar surface.

These anomalies and swirls have generated speculation both during and since the Apollo program, and their origins have not yet been settled.

Extralunar origins such as cometary impact or solar magnetic storms have been proposed, as well as lunar origins such as volcanism or alteration by gases from the lunar interior (El-Baz, 1972). Current hypotheses favor an origin resulting from magnetization of the regions antipodal to some of the major impacts on the Moon (Lin *et al.*, 1988; Hood and Williams, 1989). The origins of the swirls will probably not be resolved until these areas are actually mapped and sampled.

10.3.3. Radar Data for the Lunar Nearside

Radar-reflection data for the nearside of the Moon have been obtained using active Earth-based radio telescopes at both 3.8- and 70-cm wavelengths (Zisk *et al.*, 1974; Thompson, 1987). For any given radar measurement, two different images of the surface are generally produced (see section 9.3.2). In the region away from the *subradar point* (the point on the Moon in direct line from the radar source), the signal returned with the expected polarization sense (called the *polarized* component) produces an image of the lunar surface that appears similar to a surface illuminated by sunlight and includes highlights and shadows. In this case, however, the illumination is incident from the direction of the transmitter. A different signal, returned from the lunar surface with an opposite polarization sense (referred to as the *depolarized* component), is the result of surface scattering properties (i.e., roughness).

Radar-backscatter data for the lunar surface can be used to estimate the roughness of the surface on the scale of the wavelength (e.g., Thompson *et al.*, 1974). The intensity of radar backscatter is controlled chiefly by two sets of properties: the physical structure of the surface (i.e., amounts of blocks and craters) and the magnitude of the electromagnetic discontinuity at the surface, which is a function of the material properties (dielectric constant, loss tangent, and porosity) of the surface material. The major properties of radar-backscatter images are illustrated in the examples in Figs. 10.8–10.10. Fresh craters generally contain blocks and rubble that cause them to appear relatively rough at the scale of the radar wavelength, and they therefore appear bright in the backscatter images. A discussion of radar characteristics of lunar craters can be found in Thompson *et al.* (1974, 1979, 1980). The fine-grained regional pyroclastic (volcanic) deposits, such as the dark-mantle material sampled at the Apollo 17 site (see section 6.1.7), are generally smooth and produce very low radar backscatter. This characteristic is an important diagnostic property that allows major deposits of pyroclastic mantling material to be identified and mapped.

Fig. 10.8. Polarized radar-backscatter image of the nearside of the Moon, obtained during 1981–1984 with the 70-cm radar observatory at Arecibo, Puerto Rico (Thompson, 1987). Lunar north is at top. Since the width of the Arecibo radar antenna beam is only 10 arc-minutes (about one-third the width of the lunar disk as seen from Earth), this image is a calibrated mosaic constructed from 18 separate observations. The size of individual radar cells in the individual frames from which the image was made is 2–5 km. Dark areas correspond to individual maria with relatively smooth surfaces (e.g., Mare Crisium, on the right limb, along the first line of latitude above the equator). Bright splotches correspond to large young craters, which have blocky ejecta blankets and rays (e.g., Tycho, near the bottom center of the disk).

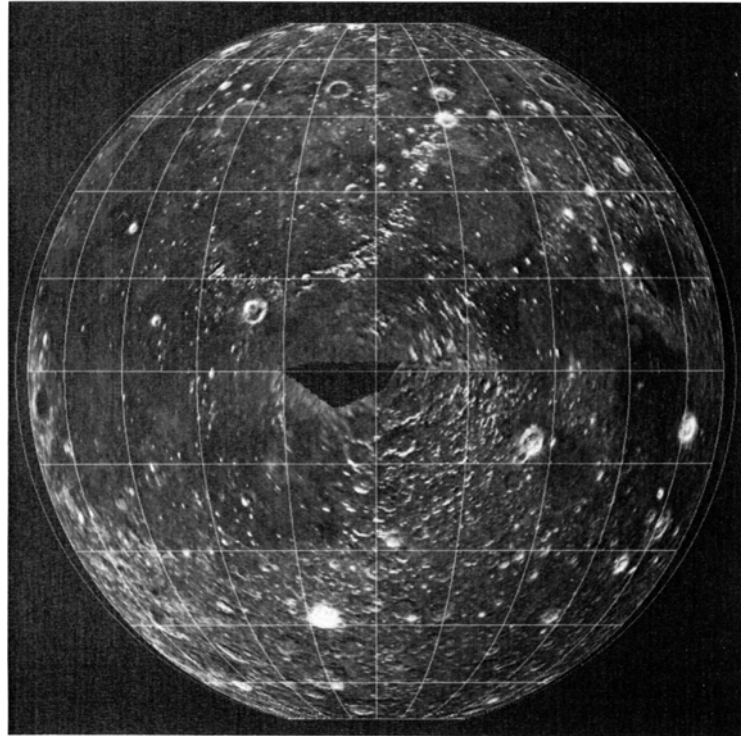
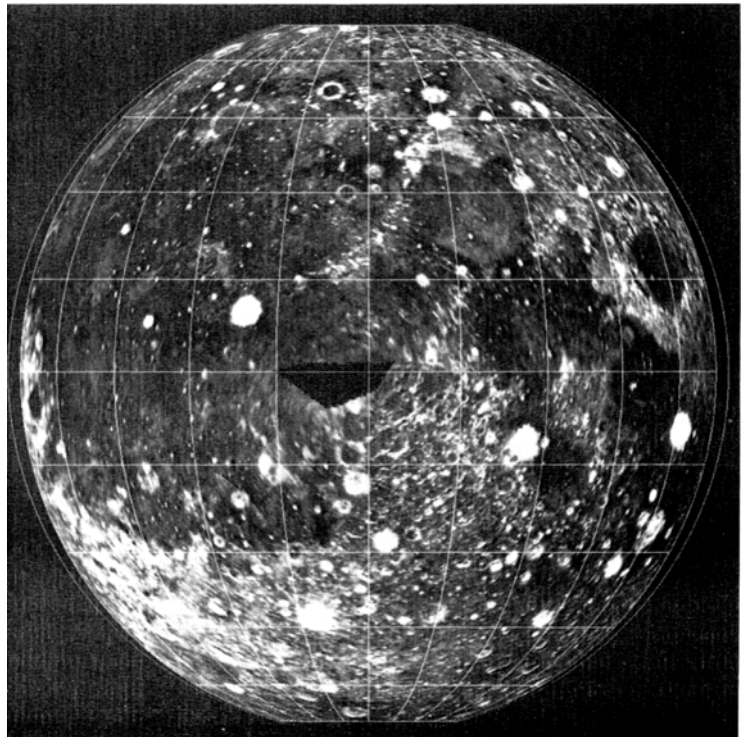


Fig. 10.9. Depolarized 70-cm radar backscatter calibrated image mosaic of the nearside of the Moon, obtained from the Arecibo radar data presented in Fig. 10.8. Lunar north is at top. In addition to high returns (bright areas) from the blocky ejecta surrounding large young craters, significant scattering differences can be observed regionally in the maria. For example, eastern Mare Tranquillitatis and western Oceanus Procellarum (center and left of lunar disk) have weaker return echoes than other maria, while the central portion of Mare Serenitatis and northern Mare Imbrium (upper center) have stronger echoes. In the highland areas on the nearside, areas near Mare Orientale (far left) have stronger echoes than do areas more distant from the Orientale Basin.



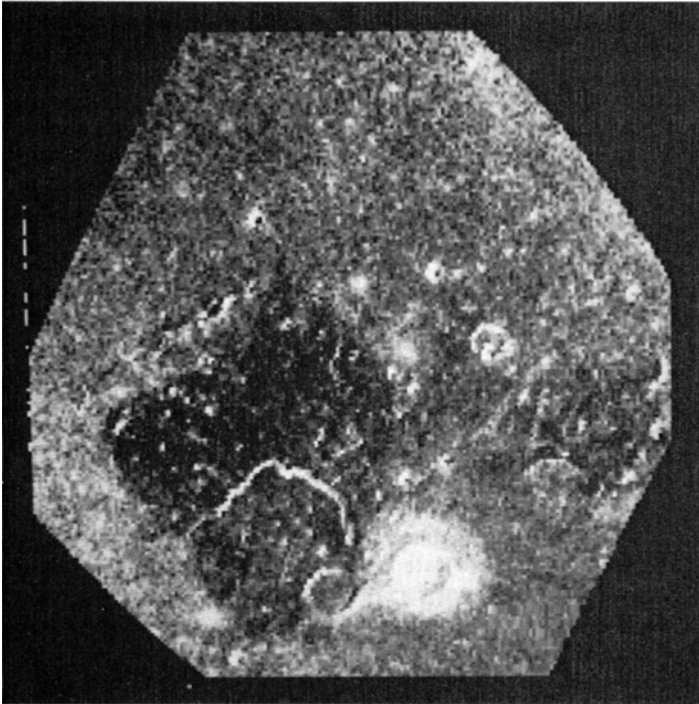


Fig. 10.10. Depolarized 3.8-cm radar backscatter image of the Aristarchus Plateau region of the Moon (ZAC reference area 6.26; Zisk *et al.*, 1974). Lunar north is at top. Radar cell size (equivalent to resolution) is about 3 km. This image provides good examples of the high backscatter from large, fresh lunar craters (bright areas), especially Aristarchus itself (large bright area at bottom), and also shows the exceptionally low backscatter from the pyroclastic deposits that cover much of the plateau (dark areas northwest of Aristarchus). The bright sinuous line west of Aristarchus is a rille (Schröter's Valley).

(Pieters *et al.*, 1973; Gaddis *et al.*, 1985). At longer wavelengths (tens of centimeters), the radar backscatter signal may in part be due to subsurface-volume scattering as well as surface-roughness scattering processes.

10.4. REGIONAL DISTRIBUTION OF LUNAR ROCK TYPES

Although coverage of the lunar surface by remotely-acquired geochemical data is limited, these data are adequate to demonstrate the compositional heterogeneity of the lunar surface. Plates 10.7–10.9 are preliminary maps showing the distribution of different rock types on the lunar surface as derived or inferred from the available remote measurements. From these data, it is clear that the Apollo and Luna collections of samples are not fully representative of the range of lunar materials exposed on the surface.

10.4.1. Mare Basalt Lavas

The compositions of lunar mare basalts from both sampled and unsampled regions of the Moon have been partially determined by using a combination of returned-sample analyses, orbital geochemical data, and Earth-based spectral reflectance measurements.

The Al/Si ratios and the Fe data obtained by orbital X-ray and gamma-ray measurements made on the Apollo 15 and 16 missions (Plates 10.4 and 10.2) clearly indicate that the maria are mafic (low Al/Si and high Fe) and are clearly distinct from the more feldspathic (higher Al/Si and lower Fe) highlands. These data indicate that the fundamental basaltic nature of the maria extends beyond the Apollo and Luna sites and that essentially all the mare regions of the Moon are composed of basaltic lava flows.

The reflectance spectra of mature mare soils, measured by optical telescopes from Earth, provide independent geochemical information at a higher spatial resolution than provided by the orbital X-ray and gamma-ray data. The lateral extent of different mare basalt types on the nearside of the Moon has been mapped at moderately-high spatial resolution (a few kilometers) using data largely acquired with Earth-based telescopes. Multispectral images in the ultraviolet (UV), visible (VIS), and near-IR (0.95 μm) wavelengths, together with albedo images of the lunar nearside and a few hundred spectral reflectance measurements of small (10 km) mare regions, were the principal data used to identify and distinguish different basalt types on the Moon (see review in Pieters, 1978).

Multispectral images in the blue to visible part of the spectrum (0.35 to 0.7 μm) are particularly sensitive to the Ti content of mare soils (e.g., *Charette et al.*, 1974), and a map of lunar basalt types based on inferred Ti content is shown in Plate 10.7. Units are distinguished in terms of estimated Ti content of the soil, based on UV/VIS color ratios and albedo; these estimated Ti concentrations are in qualitative agreement with the lower-resolution orbital data shown in Plate 10.3. Furthermore, the type and abundance of mafic minerals (pyroxenes, olivine, and/or Fe-rich glass) can be independently estimated from variations in absorption features near 1.0 and 2.0 μm (see section 6.2.1), and these quantities can be used to further distinguish lunar basalt types. Blue tones in Plate 10.7 are assigned to relatively Ti-rich soils, red tones indicate relatively Ti-poor soils, and intermediate tones represent soils intermediate in Ti content. Regions of volcanic pyroclastic material (shaded tones), which often mantle highlands near the edges of maria, are identified by their generally low albedo, their exceptionally low radar backscatter, and the frequent presence of a broad glass absorption band (from Fe^{2+}) near 1.0 μm (*Pieters et al.*, 1973; *Adams et al.*, 1975; *Gaddis et al.*, 1985).

From these data it is clear that the maria are heterogeneous, and there appear to be regional differences in chemical composition and in the ages estimated remotely from crater-count data (Plate 10.11). No mare basin is filled with a single type of basalt. Although some series of similar or related basalt flows are extensive, every mare basin or other large region filled with basalt shows a variety of basalt compositions within areas only a few hundred kilometers across.

From the stratigraphic relations deduced from photogeologic studies, it is clear that older basalts often have different compositions than younger ones. The unsampled Ti-rich basalts of Oceanus Procellarum (labelled HDSA and hDSA in Plate 10.7), for example, are superposed on extensive older, low-Ti basalts. These high-Ti basalts in Oceanus Procellarum are among the youngest on the Moon (*Boyce*, 1976), but they are distinct from the Ti-rich basalts of the Moon's eastern hemisphere (e.g., the Apollo 11 basalts, HDWA in Plate 10.7), and they are probably enriched in olivine (*Pieters et al.*, 1980). It is estimated that about two-thirds of the distinct basalt types on the nearside of the Moon have not yet been sampled (*Pieters*, 1978).

10.4.2. Petrologic Map of the Moon from Apollo Gamma-ray Data

It is possible to combine the three Apollo gamma-ray chemical maps (for Th, Fe, and Ti) into a single map showing the distribution of petrologic provinces

on the Moon. *Davis and Spudis* (1985) showed that a plot of orbital chemical data for the Th/Ti ratio against Fe (shown in Plate 10.8a) made it possible to recognize three major lunar rock types across a large fraction of the lunar globe: ferroan anorthosites, mare basalts, and the group of KREEP/Mg-suite norites. These geochemical discriminators are similar to the groupings produced by the systematics of Ti/Sm vs. Mg/(Mg + Fe) ratios used in some studies of pristine highland rocks (*Longhi and Boudreau*, 1979; *Norman and Ryder*, 1980a,b), although the latter ratios were designed to show the effects of ilmenite fractionation in early lunar crustal differentiation.

The fact that the Th/Ti vs. Fe relations (Plate 10.8a) distinguish three major lunar rock types can be used (*Davis and Spudis*, 1987) to reduce all the orbital chemical data to a triangular (ternary) plot of these major rock types. In such a plot, the value of each surface measurement (pixel) of chemical data is included in a ternary space defined by the apices FAN (ferroan anorthosite), MB (mare basalt), and MG (Mg-suite/KREEP) (cf. Plates 10.8b,c). By assigning the three primary colors (red, green, and blue) to the apex components of this ternary plot, the distribution of zones of both "pure" rock types and intermediate compositions can be shown across the Moon (Plates 10.8d,e).

The lunar petrologic map of Plate 10.8 shows that the bulk of the highlands along the Apollo 15 and 16 groundtracks are anorthosite-rich (predominance of blue colors), although other specific petrologic regions are also evident. In fact, the orbital data indicate that the highlands are petrologically heterogeneous and have had a complex evolution, probably involving continuing intrusive activity, deposition of ejecta from large impact basins, and volcanic resurfacing (*Davis and Spudis*, 1985, 1987; *Spudis and Davis*, 1986). The Fe-rich maria are evident as greenish colors, although most mare deposits also show the chemical effects of admixture of highland debris (greenish-cyan colors). For details on this petrological mapping technique, see *Davis and Spudis* (1985, 1987).

10.4.3. Mineralogy of Highland Rock Types Inferred from Near-Infrared Reflectance Spectra

Characteristic near-IR absorption features in the wavelength range 0.90–1.3 μm are diagnostic of various types of pyroxene, olivine, plagioclase, and glass (see sections 6.2.1 and 6.5). These features can be used to identify the presence of these minerals from remotely-acquired reflectance spectra of lunar surface materials. With sufficiently high precision and adequate spectral resolution, mineral abundances can be estimated and thus the rock types

exposed at the surface can be identified (e.g., *Pieters and Mustard*, 1988).

Because of the strongly absorbing nature of soil agglutinates (see section 7.3), absorption features are most readily examined in the reflectance spectra obtained from freshly exposed surfaces, such as those that occur in fresh craters or on steep slopes. Near-IR reflectance spectra have been obtained for freshly-exposed material in almost 100 small lunar regions, each 3–5 km in diameter. Various amounts of low-Ca orthopyroxene, high-Ca clinopyroxene, olivine, and plagioclase have been identified from spectra of these areas (*Pieters*, 1986; see Figs. 6.45 and 6.46) using Earth-based telescopes.

The heterogeneity of the lunar crust can be evaluated by spectral reflectance studies of relatively fresh surfaces exposed by craters. In addition, vertical as well as lateral variability among the crustal rocks can be determined by using the sizes of craters to estimate the original depth of material excavated (*Pieters*, 1986). More than 75% of moderately small highland craters (<15 km in diameter) are dominated by rock types with low-Ca pyroxene as the major mafic mineral, although there are variations in the spectra due to degree of brecciation and pyroxene abundance. Although limited by the number of measurements available, these observations imply that the upper 1–2 km of the lunar highland crust, which is roughly equivalent to the zone often referred to as *megaregolith*, is dominated by a variety of noritic compositions.

Larger craters (>50 km in diameter) probe deeper and, in contrast, excavate a surprising diversity of materials. Evaluation of compositional variations with depth is accomplished by examining different depositional regimes across a crater; for large craters, this type of analysis is within the spatial-resolution capabilities of Earth-based telescopes. The central peaks of large impact craters represent material excavated from the greatest depth (one-sixth to one-tenth the crater diameter), whereas materials forming the rim and the ejecta deposits represent higher stratigraphic units. Crustal stratigraphies reconstructed in this manner are shown in Plate 10.9 (*Pieters*, 1989). In addition to documenting the diversity of lunar crustal materials, these data also provide information on the expected range of materials represented in the returned lunar samples. Noritic (low-Ca pyroxene) and anorthositic (very feldspar rich) compositions dominate the regions surrounding the sampling sites. The occurrence of gabbroic rock types (with high-Ca pyroxene) and the less common troctolites (very olivine-rich), on the other hand, are particularly concentrated in the poorly sampled western hemisphere (*Pieters*, 1986; *Lucey and Hawke*, 1988).

10.5. STRATIGRAPHY AND RELATIVE AGES

The Moon has been mapped geologically at a wide variety of scales. The principles of stratigraphy as applied to lunar history are discussed in section 4.4. *Wilhelms* (1987) has summarized our current knowledge of lunar stratigraphy in the form of an abstract global geologic map (Plate 10.10). On this map, rock-stratigraphic units are subdivided into basin, crater, plains, and mare units. Time-stratigraphic classification (discussed in section 4.4) is indicated for the pre-Nectarian through Copernican systems.

The quantitative study of lunar crater morphology (*morphometry*) and crater density in the lunar maria has permitted subdivision of mare units in terms of relative age (*Boyce*, 1976; *Boyce and Johnson*, 1978; *BVSP*, 1981). A relative age map of the lunar maria is shown in Plate 10.11. This map combines data for the relative ages of mare basalts, obtained from both the so-called “D_i” method (*Soderblom and Lebofsky*, 1972; *Boyce*, 1976) and the cumulative crater density method (*Boyce and Johnson*, 1978). These relative ages are then converted to estimates of absolute ages by comparison to actual age measurements made through isotopic studies of returned basalt samples from the Apollo and Luna landing sites (*Boyce*, 1976).

10.6. GEOLOGY OF THE APOLLO AND LUNA LANDING SITES

Six manned Apollo missions and three robotic Luna missions returned samples from several geologic settings on the Moon. In particular, the later Apollo missions (15–17; the “J” missions) explored increasingly complex geologic terrains. The purpose of this section is to briefly review the regional and local geologic setting of each landing site and to present an interpretive geologic cross-section based on current (and clearly incomplete) understanding.

10.6.1. Apollo 11

The first lunar landing mission, Apollo 11, sampled the relatively old, Ti-rich (“blue”) lunar maria in southwestern Mare Tranquillitatis (landing site: 0.7°N, 24.3°E; Fig. 10.11). The site for the first lunar landing was chosen primarily for safety (relatively flat terrain; few large boulders). This mission provided our first look at the lunar maria, and analysis of the returned samples confirmed the theory that the maria are composed of basaltic lava flows. One “extravehicular activity” (EVA) traverse of two-and-one-half hours was performed by the astronauts on foot (Fig. 10.12).

The Apollo 11 landing site is no closer than about 40 km to the nearest mare/highland boundary, but a significant fraction (a few percent) of the returned regolith samples consists of feldspathic lithic and mineral fragments that were postulated (and subsequently shown) to be derived from highland areas (Wood *et al.*, 1970). The mare basalts range in age from 3.88 to 3.57 b.y. (Sm-Nd ages; BVSP, 1981). These ages are ancient by terrestrial standards, but they are generally younger than the ages inferred for the large multiring basins, whose ejecta deposits were sampled on later missions (e.g., Imbrium; ~3.85 b.y.). At least two chemically distinct groups of basalts of differing ages are present, suggesting the presence of at least two different lava flows in the vicinity of the site. These relations are summarized in the cross-section of Fig. 10.13. More detailed discussions of the geology of the Apollo 11 site are found in Shoemaker *et al.* (1970a) and Beatty and Albee (1978, 1980).

10.6.2. Apollo 12

The Apollo 12 mission was also sent to a relatively flat mare site for safety reasons, but it was the first mission to demonstrate pinpoint landing capability by landing within 200 m of the Surveyor 3 spacecraft in southeastern Oceanus Procellarum (landing site: 3.2°S, 23.4°W; Fig. 10.14). This region of the Moon consists of mare basalts that are lightly cratered relative to those at the Apollo 11 site (hence younger) and of a slightly more “reddish” color (hence different in composition). Some distal ejecta rays from the large Copernicus Crater (400 km to the north) cross the site, leading scientists to hope that this material could be sampled and age-dated to determine the actual time of formation of Copernicus. None of the samples returned, however, could be proven to be from Copernicus. Two EVA traverses on foot were made during this mission (Fig. 10.15).

Samples from the Apollo 12 site indicate the presence of at least three chemically distinct groups of mare basalts ranging in age from 3.29 to 3.08 b.y. (BVSP, 1981). The enigmatic KREEP component was first recognized in the Apollo 12 samples in the form of dark, agglutinitic glasses and a complex polymict breccia (sample 12013). Petrologic and geologic studies of the Apollo 12 site have been used to prepare a tentative cross-section (Fig. 10.16). Detailed discussion of the geology of the Apollo 12 site can be found in Shoemaker *et al.* (1970b), Warner (1970b), Rhodes *et al.* (1977), and Wilhelms (1984).

10.6.3. Apollo 14

The Apollo 14 mission was sent to a hilly region north of Fra Mauro Crater (landing site: 3.7°S, 17.5°W; Fig. 10.17). This landing site was the first in

the lunar highlands, and it was chosen partly because it was believed to contain ejecta from the nearby Imbrium Basin. The Imbrium impact event serves as a major boundary to subdivide lunar geologic history (see section 4.4), and the science objectives for the Apollo 14 mission included both the determination of the absolute age of the Imbrium impact and the examination of the Imbrium Basin ejecta, which was thought to have been derived from deep within the highland crust. Two EVA traverses on foot were performed (Fig. 10.18).

Rocks returned by the Apollo 14 mission included complex polymict fragmental breccias, impact-melt breccias, and clast-poor impact melts with generally basaltic and KREEP-rich compositions; these polymict samples were assembled into their present forms about 3.8 to 3.9 b.y. ago. Their origin still remains contentious. Post-Apollo studies have shown that basin ejecta deposits consist in general of a mixture of primary basin ejecta and admixed local material, although the exact proportions are unknown (cf. Oberbeck, 1975; Schultz and Gault, 1985). As a result, it is still unclear which rocks from the Apollo 14 site represent true Imbrium Basin ejecta; a noncommittal cross-section is presented in Fig. 10.19. The geology of the Fra Mauro (Apollo 14) region is discussed in detail by Chao (1973), Swann *et al.* (1977), Hawke and Head (1977), and Simonds *et al.* (1977).

10.6.4. Apollo 15

Apollo 15 was the first advanced (“J”) mission and the first to be sent to a complex, multiple-objective landing site, the Hadley-Apennine region (landing site: 26.1°N, 3.7°E; Fig. 10.20). This site was chosen to sample and investigate (1) the massifs and highlands that form the rim of the Imbrium Basin and (2) the mare lavas and landforms (e.g., Hadley Rille) of Palus Putredinis. Three extended EVAs were performed (Fig. 10.21), an advance made possible by the first use of the Lunar Roving Vehicle (LRV; see section 9.1.11).

The mare surfaces at the Apollo 15 site provided samples of basaltic lavas of two distinct chemical groups (quartz normative and olivine normative); both groups have virtually the same age (3.3 b.y.). The highland material collected consists of a variety of rock types: anorthosites, Mg-suite plutonic rocks, impact melts, and granulites. Many of these rocks occur as individual clasts in regolith breccias collected from the highland areas at the site. Results from the Apollo 14 and 15 missions together indicate that the Imbrium Basin formed about 3.85 b.y. ago. Two surprising volcanic materials were discovered at the Apollo 15 site: an aluminous, nonmare basalt, rich in KREEP, and an emerald-green glass of

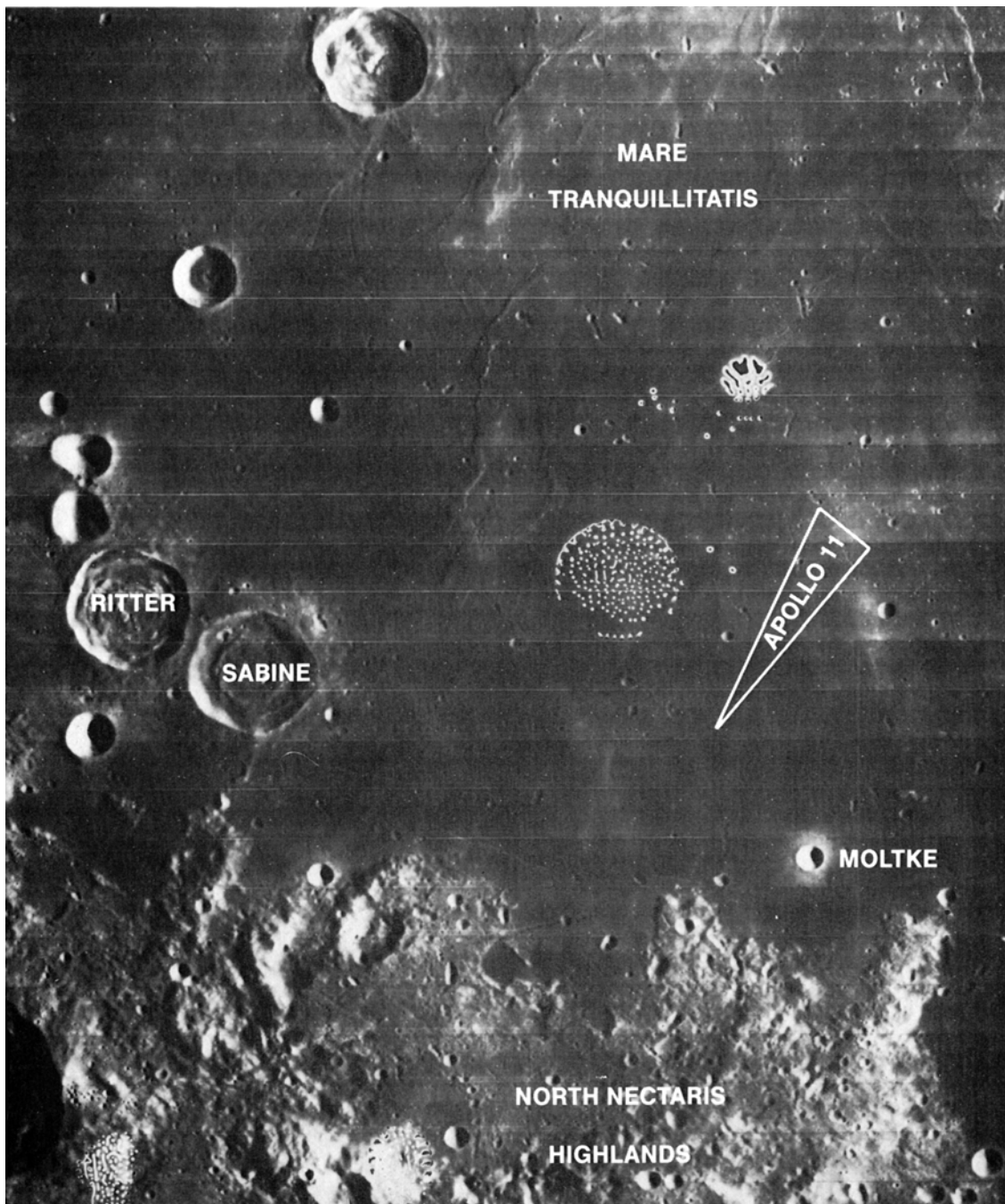


Fig. 10.11. Regional view of southwestern Mare Tranquillitatis, including the Apollo 11 landing site. Lunar north is at top. The actual landing site is on mare basalts of a bluish color and a relatively high crater density (old, high-Ti basalts). The nearest highlands are the circum-Nectaris massifs (bottom), approximately 40 km south of the Apollo 11 site. Horizontal lines are framelet boundaries in this Lunar Orbiter photograph. Each framelet is 12 km wide. The white blemish above the Apollo 11 landing site is a flaw in the film developed in the Lunar Orbiter spacecraft. (NASA Photo LOIV-85H1.)

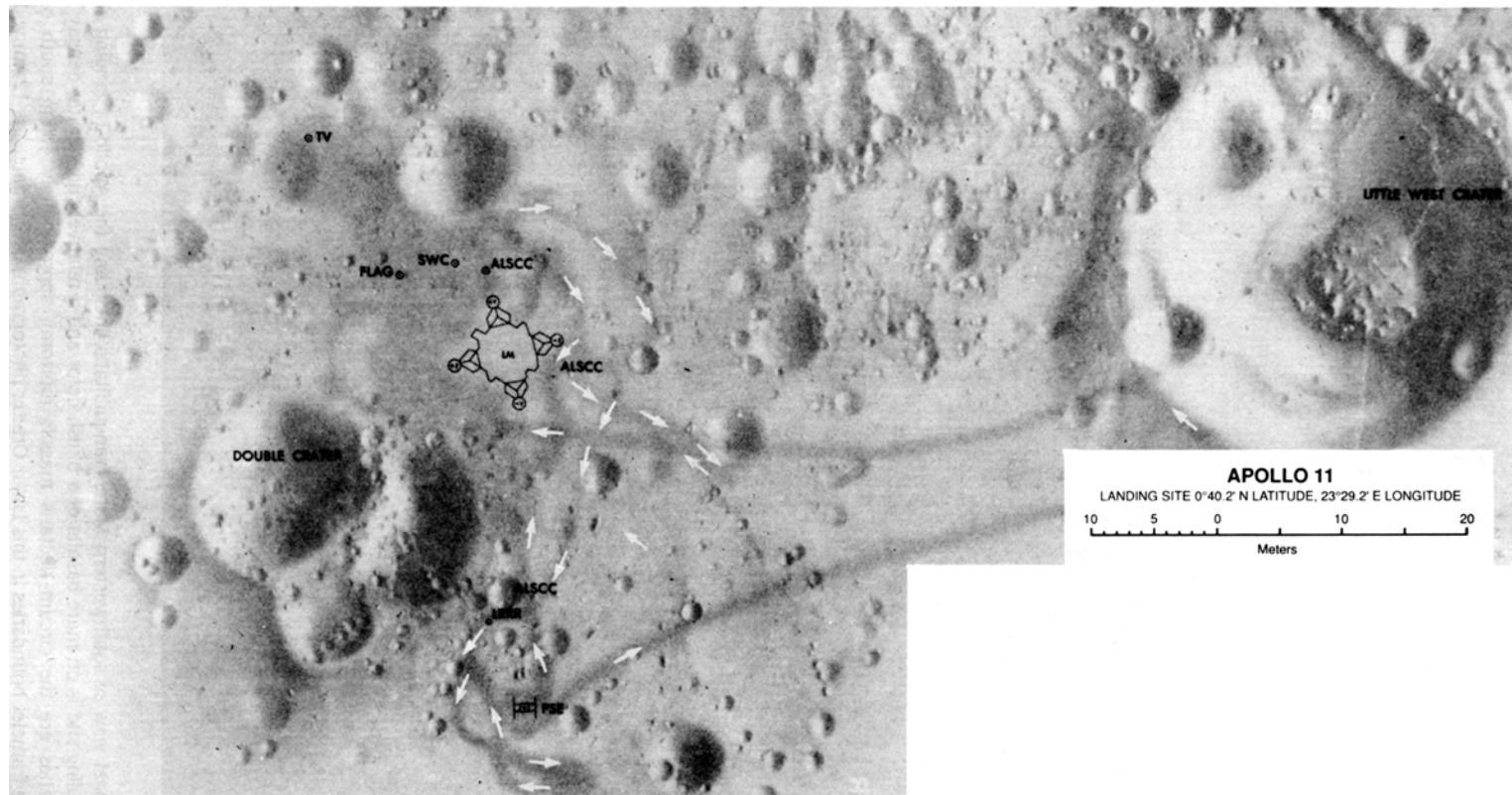


Fig. 10.12. Apollo 11 site traverse map, showing locations of the Lunar Module (LM) and deployed surface experiments. Probable astronaut traverses are shown by the white arrows. (From Defense Mapping Agency; original scale 1:250.) ALSCC = Apollo Lunar Surface Close-up Camera; SWC = Solar-Wind Composition Experiment; PSE = Passive Seismic Experiment; LRRR = Laser Ranging Retroreflector; TV = Television Camera.

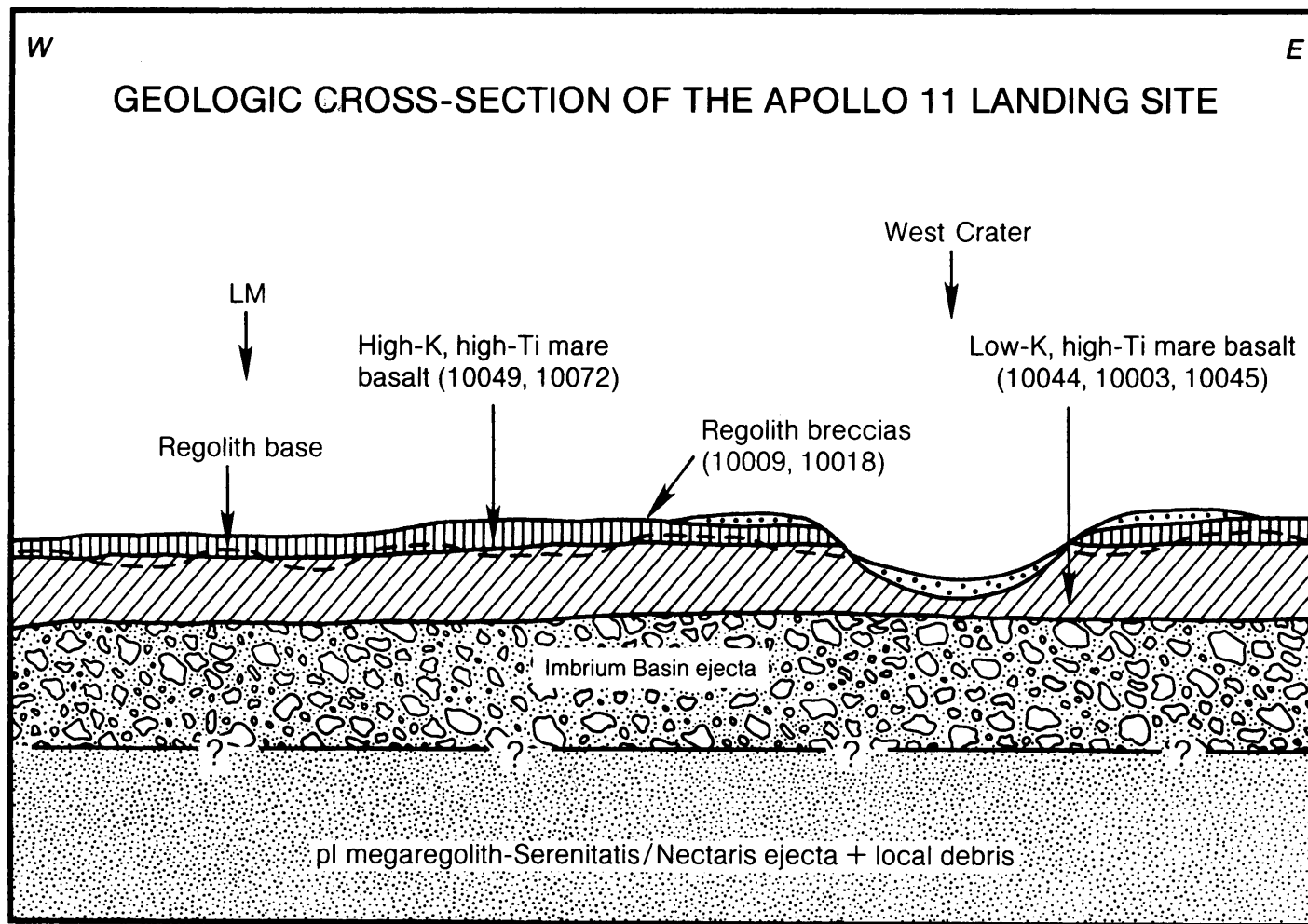


Fig. 10.13. Schematic east-west geologic cross-section through the Apollo 11 landing site, showing at least two basalt lava flow units overlying older ejecta from major impact basins (modified after *Beaty and Albee, 1980*). Presence of the Imbrium ejecta layer is inferred. Numbers refer to specific collected samples representative of the various units inferred to be present. The base of the regolith (dashed line) locally penetrates into the low-K mare basalts. Abbreviation “pl” stands for pre-Imbrian in the deep megaregolith.

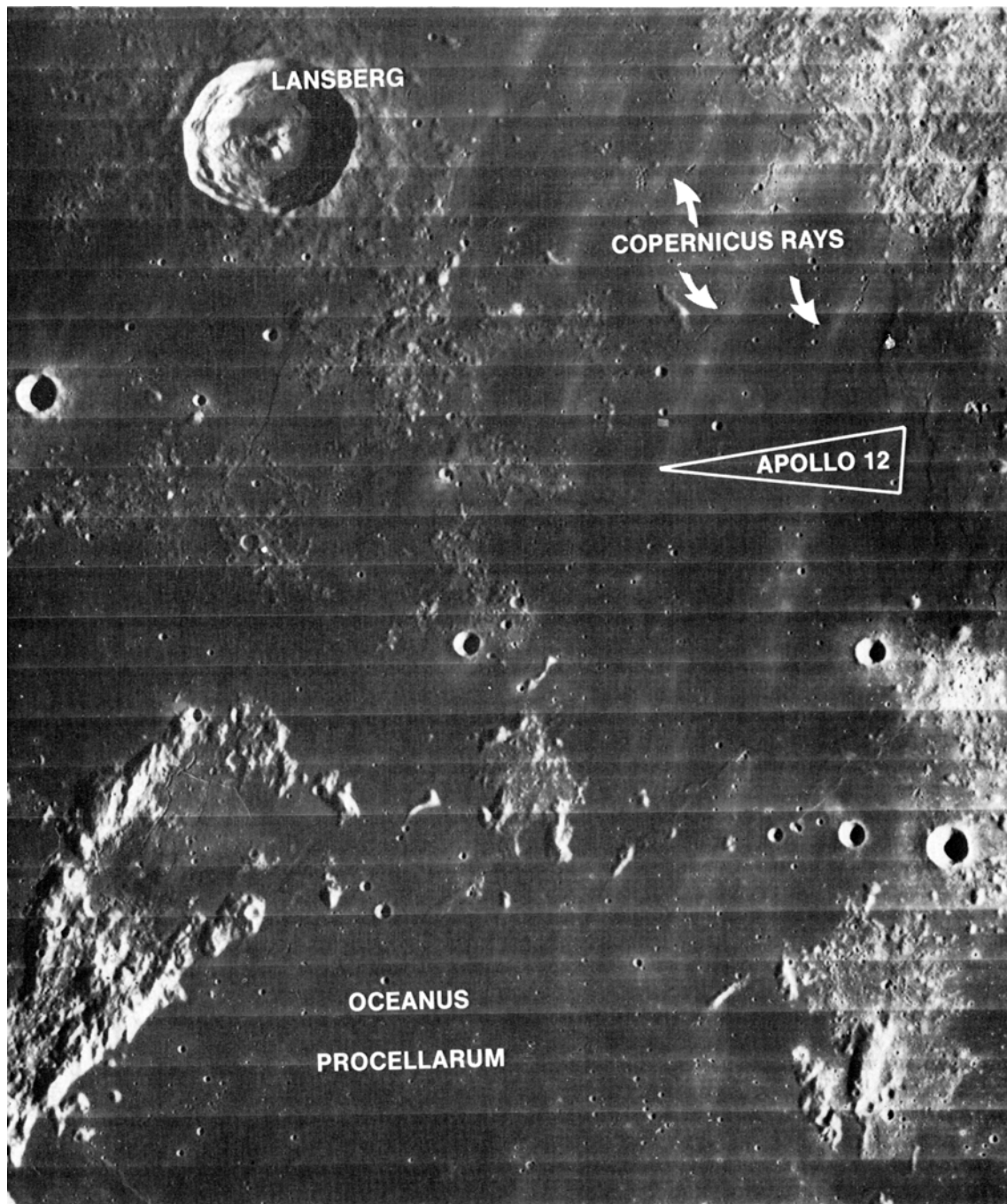


Fig. 10.14. Regional view of southeastern Oceanus Procellarum, showing the Apollo 12 landing site. Lunar north is at top. The actual landing site is on mare basalt with a relatively reddish color and a relatively low crater density (i.e., young, low-Ti basalts). Exposed islands of highland material (light-colored) in the mare suggest that the mare basalt in this region is relatively thin. Rays from Copernicus Crater (light-colored) cross the landing site from northeast to southwest. Horizontal lines are framelet boundaries in this Lunar Orbiter photograph. Each framelet is 12 km wide. (NASA Photo LOIV-125H3.)

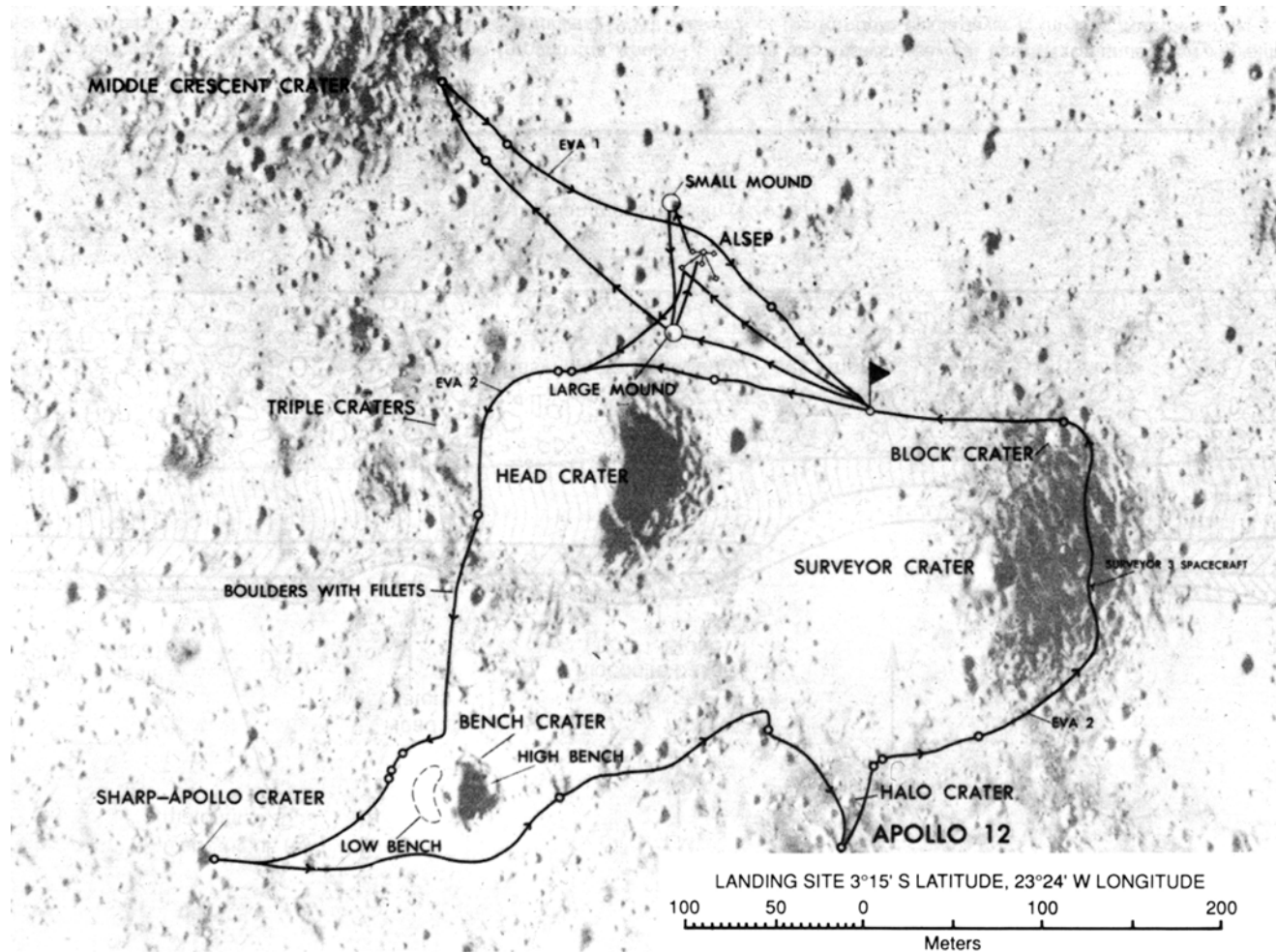


Fig. 10.15. Apollo 12 site traverse map, showing topographic features and scientific sites. The Lunar Module (LM) landing site is shown by the flag on the north rim of Surveyor Crater. The Surveyor 3 spacecraft landed on the east rim of this crater. Solid lines indicate astronaut traverses (extravehicular activity or “EVA”). (From Defense Mapping Agency; original scale 1:2500.) ALSEP = Apollo Lunar Surface Experiments Package.

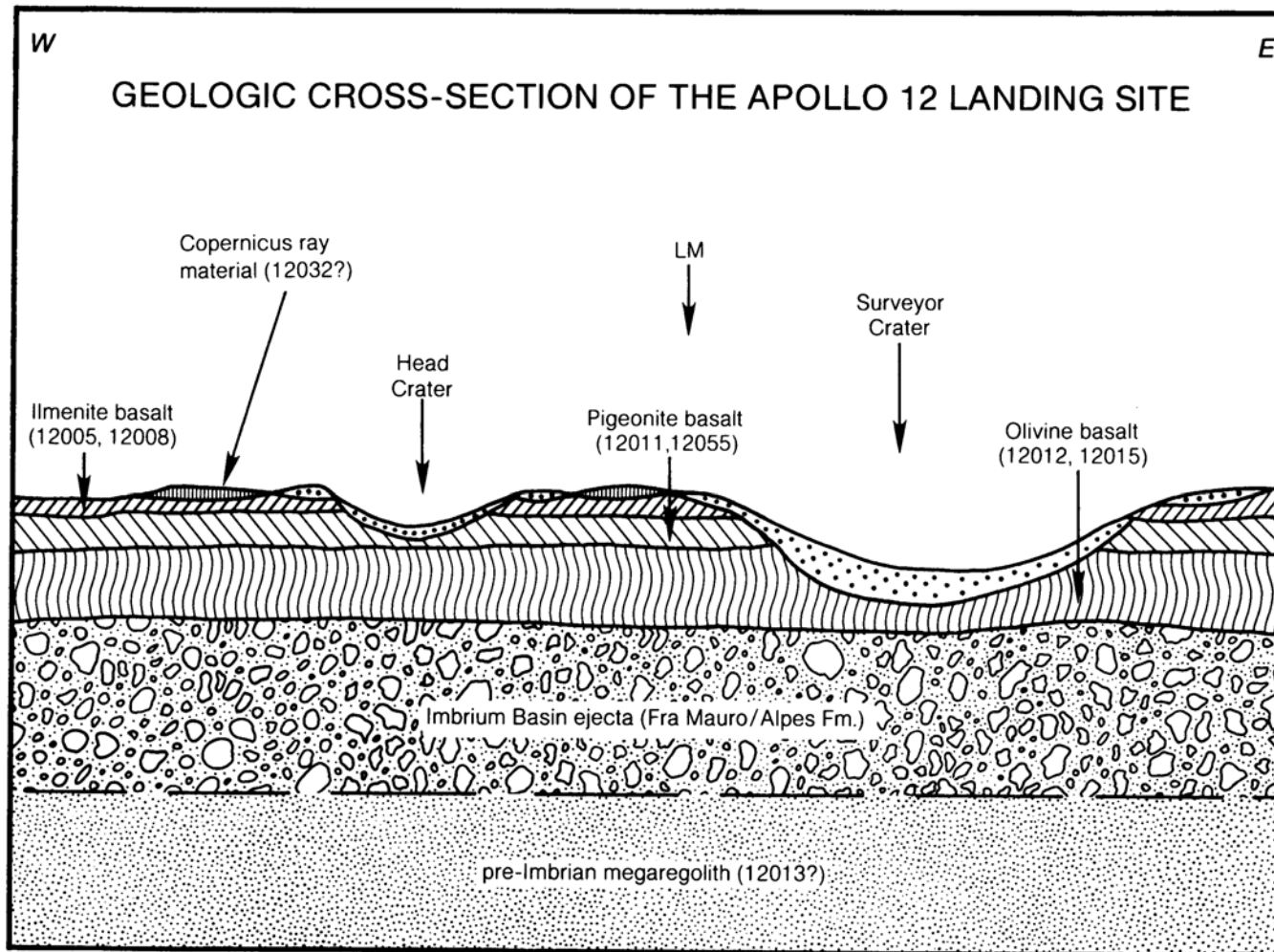


Fig. 10.16. Schematic east-west geological cross-section through the Apollo 12 landing site showing several basalt lava units overlying older ejecta from major impact basins (modified after *Rhodes et al., 1977; Wilhelms, 1984*). Presence of the Imbrium ejecta layer is inferred. Numbers refer to specific collected samples representative of the various units inferred to be present.



Fig. 10.17. Regional view of the Fra Mauro highlands, showing the Apollo 14 landing site. Lunar north is at top. The actual landing site is on hummocky material (the Fra Mauro Formation) that overlies the pre-Imbrian Fra Mauro Crater; this material is apparently ejecta that was deposited during formation of the Imbrium Basin. Horizontal lines are framelet boundaries in this Lunar Orbiter photograph. Each framelet is 12 km wide. (NASA Photo LOIV-120H3.)

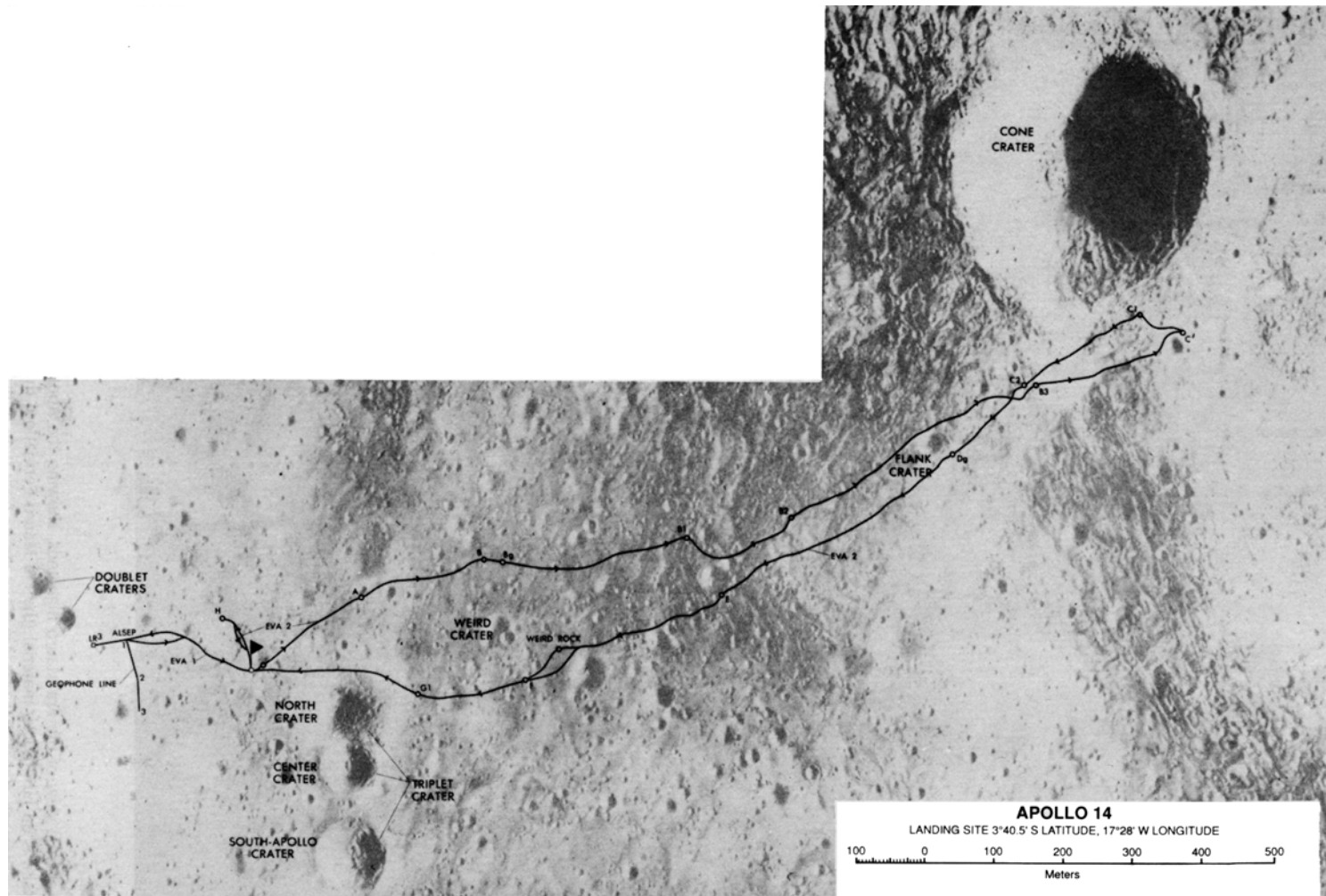


Fig. 10.18. Apollo 14 site traverse map, showing topographic features, scientific sites, and astronaut traverses (solid lines). The Lunar Module (LM) landing site is shown by the flag at the left side. (From Defense Mapping Agency; original scale 1:4000.) Letters are sampling/photo stops; ALSEP = Apollo Lunar Surface Experiments Package; EVA = extravehicular activity.

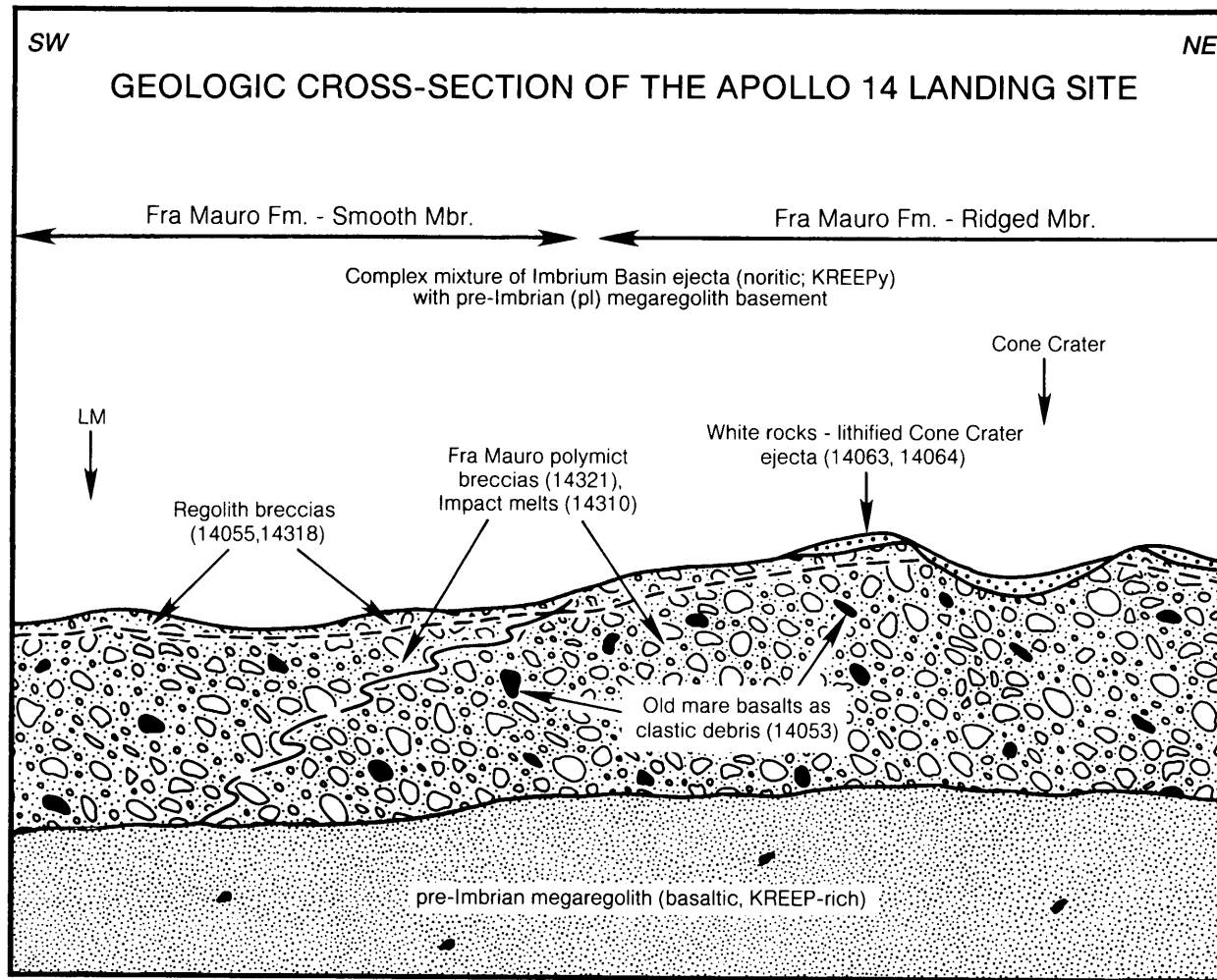


Fig. 10.19. Schematic east-west geologic cross-section through the Apollo 14 landing site, showing contact between “smooth” and “ridged” members (Mbr.) of the Fra Mauro Formation, which is an assemblage of complex impact-produced breccias (after Swann *et al.*, 1977). Numbers refer to specific collected samples that are representative of the units inferred to be present. LM shows where the Lunar Module landed. Dashed line below surface represents the depth of regolith.

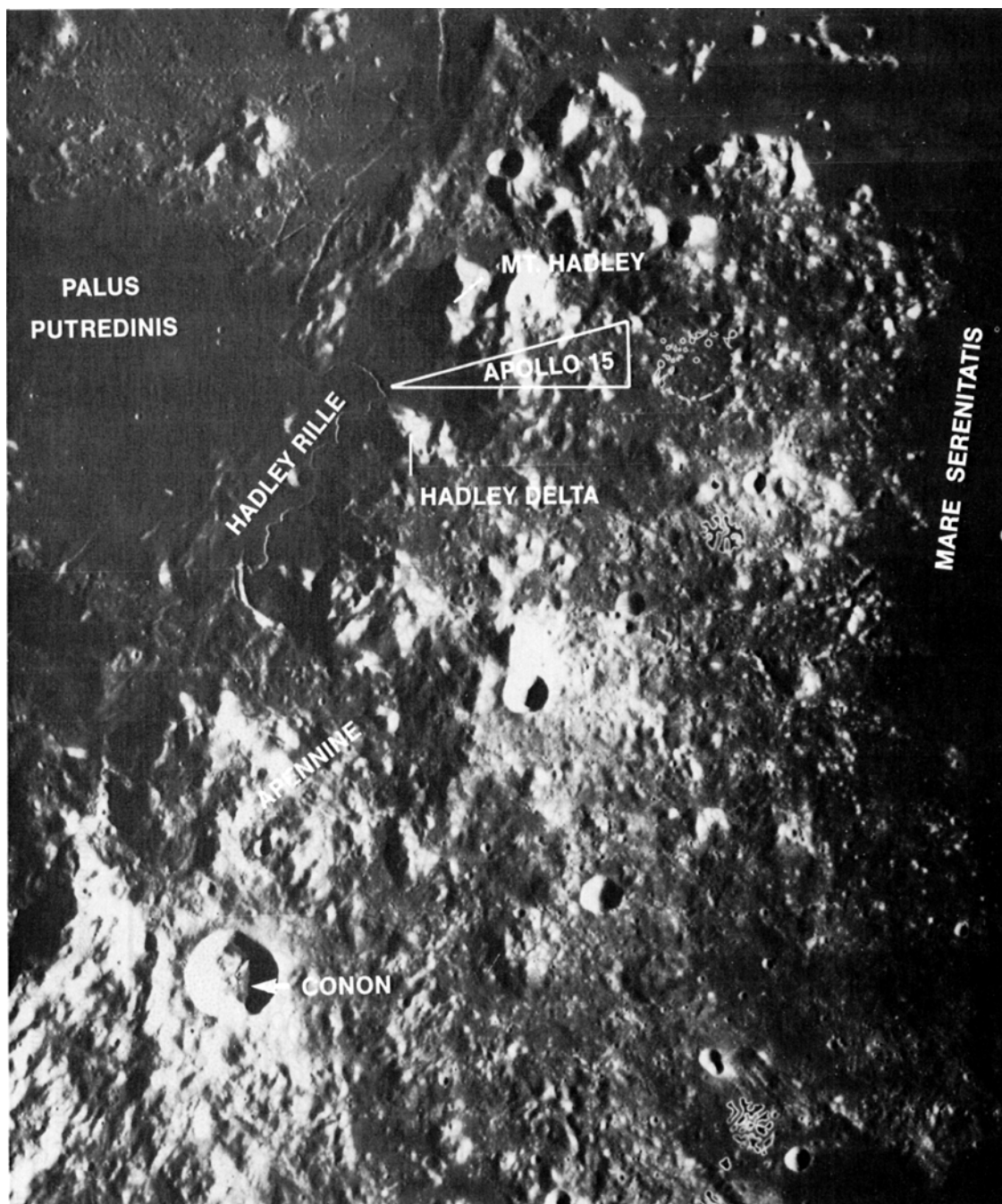


Fig. 10.20. Regional view of the southeastern edge of Mare Imbrium, showing the highland-mare boundary in the Hadley-Apennine area and the Apollo 15 landing site. Lunar north is at top. The actual landing site is located on the reddish (low-Ti) mare basalts of Palus Putredinus, adjacent to the Apennine Scarp, which is part of the main rim of the Imbrium Basin. Hadley Rille is a sinuous rille that runs across the mare material. Horizontal lines are framelet boundaries in this Lunar Orbiter photograph. Each framelet is 12 km wide. Conon Crater is 22 km in diameter. (NASA Photo LOIV-102H3.)



Fig. 10.21. Apollo 15 site traverse map, showing topographic features, scientific sites, and astronaut traverses (solid lines). The Lunar Module landing site is approximately in the center of the picture, on the flat area of mare basalts. Hadley Rille (Rima Hadley) runs along the left side of the picture, and the highland massif (the Apennine Scarp; here called Hadley Delta) is at the bottom. (Defense Mapping Agency Chart 41B4S4(25); original scale 1:25,000.)

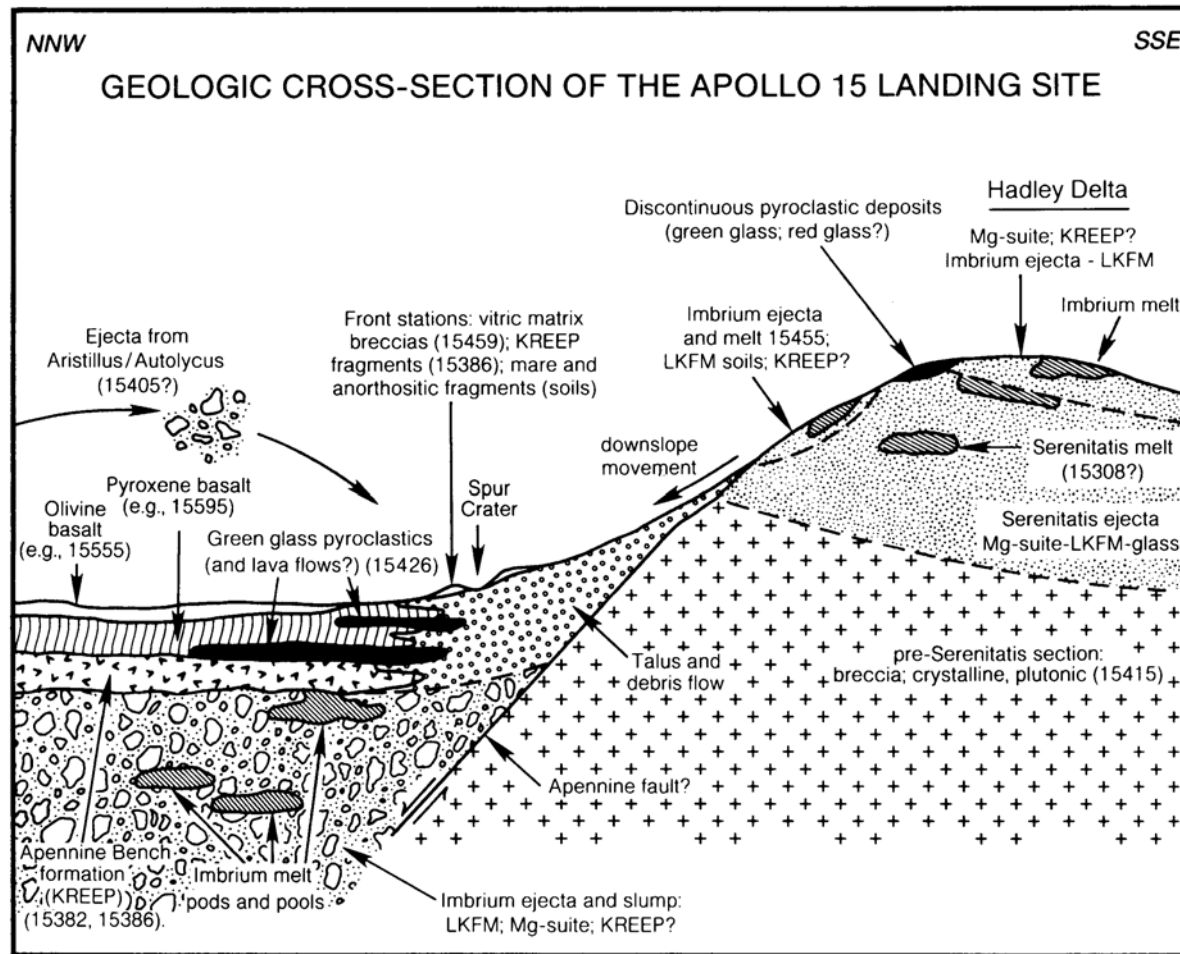


Fig. 10.22. Schematic northwest-southeast geologic cross-section through the Apollo 15 landing site, showing the complex geological transition between mare and highlands (modified from *Spudis and Ryder, 1985; Swann et al., 1972; Swann, 1986*). In the mare (left), post-Imbrian basalt lavas overlie a thick deposit of Imbrium ejecta. In the highland area (Hadley Delta, right), older (pre-Imbrian) ejecta from Mare Serenitatis overlies lunar crustal rocks. Numbers refer to specific collected samples that are representative of the various units inferred to be present.

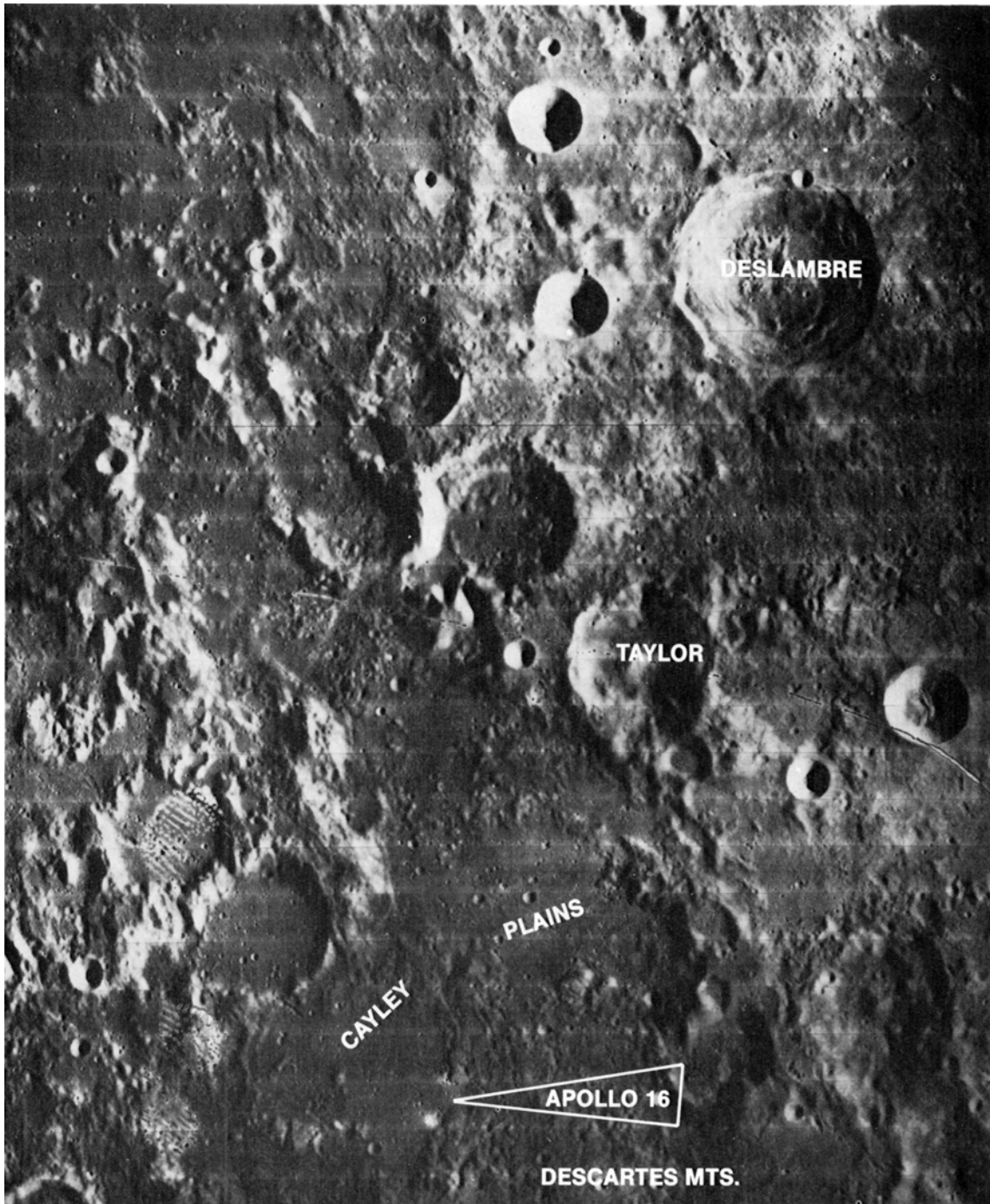


Fig. 10.23. Regional view of the Descartes Highlands, showing the Apollo 16 landing site. Lunar north is at top. Rough, light-colored material near the bottom of frame, making up the Descartes Mountains, is the Descartes Formation, which is interpreted as ejecta from the older Nectaris Basin. The smooth, intermontane plains (darker) are the Cayley Formation, once thought to be a volcanic unit but now interpreted as ejecta from another impact basin (Imbrium?). Horizontal lines are framelet boundaries in this Lunar Orbiter photograph. Each framelet is 12 km wide. Blemishes in the lower left corner are flaws in the film developed in the Lunar Orbiter spacecraft. (NASA Photo LOIV-89H3.)

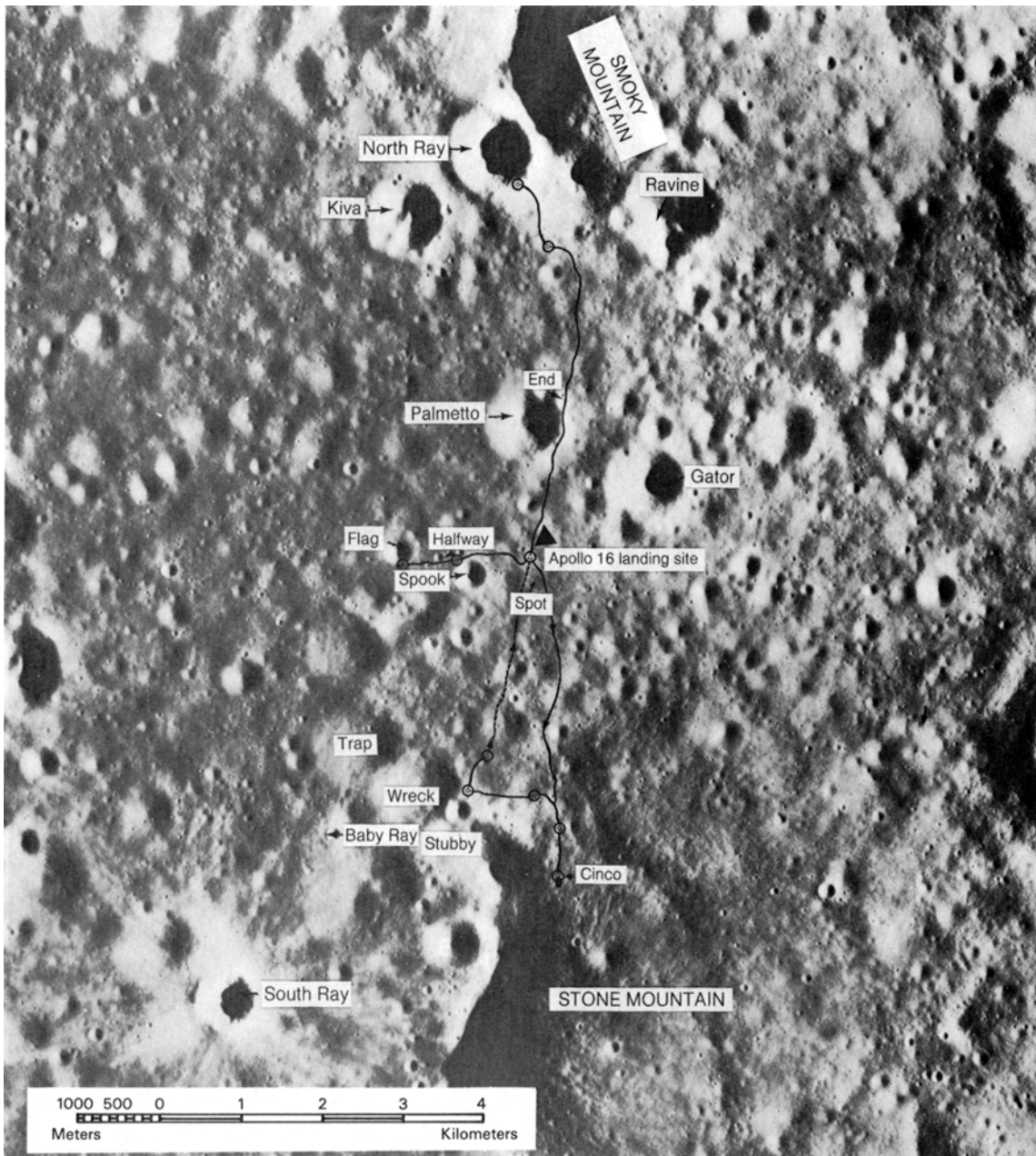


Fig. 10.24. Apollo 16 site traverse map, showing topographic features, scientific sites, and astronaut traverses. Solid lines are used where the traverse is known, dashed lines where the traverse is approximate. The Lunar Module landing site is about in the center of the picture, on the more level plain of the Cayley Formation. This unit was sampled during a short traverse west of the landing site. Longer traverses to north and south sampled the more rugged Descartes Formation at Smoky Mountain/North Ray Crater (north) and at Stone Mountain (south). (Defense Mapping Agency Chart 78D252(25); original scale 1:25,000.)

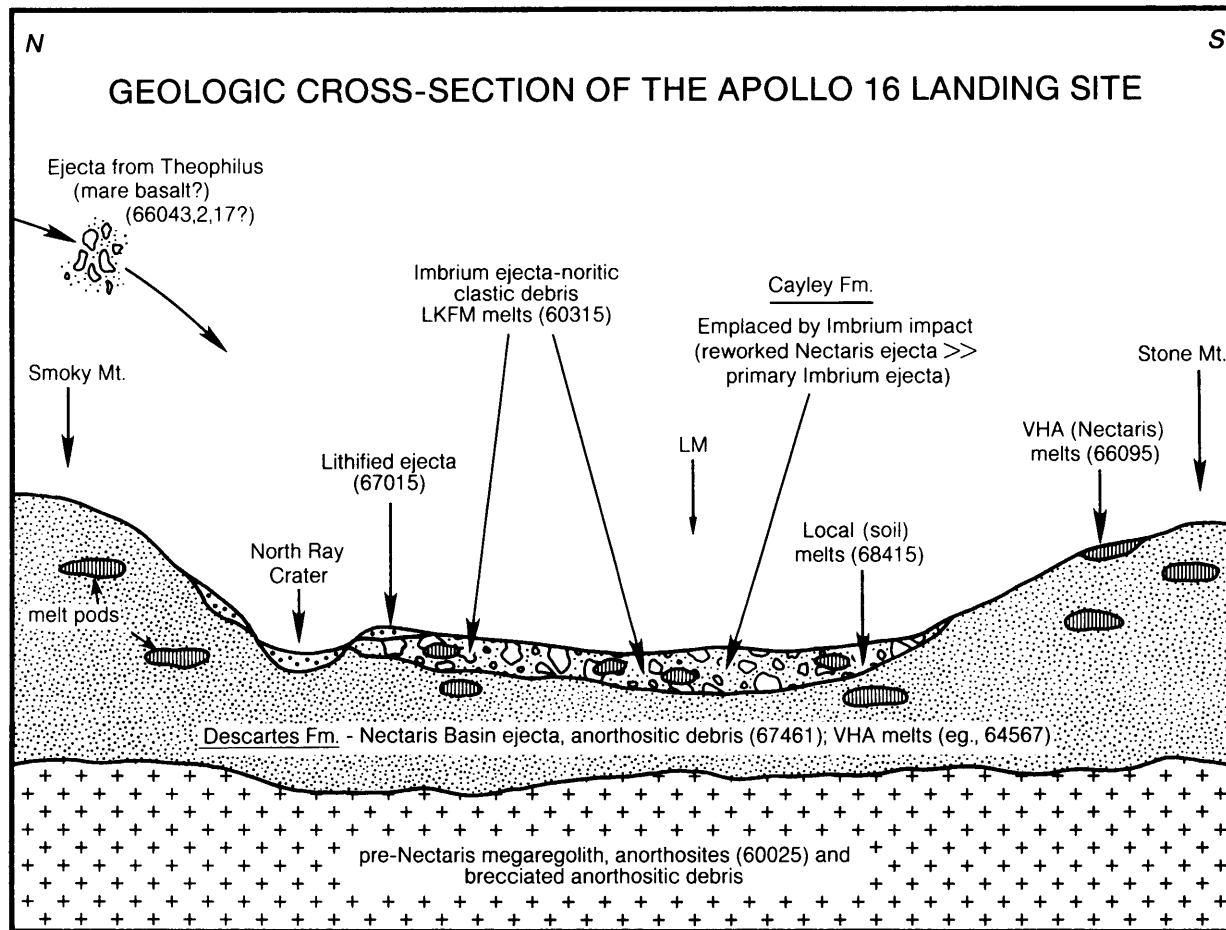


Fig. 10.25. Schematic geologic cross-section through the Apollo 16 landing site, showing the complex interrelations of different units of impact-produced ejecta excavated from large mare basins (modified after *Spudis, 1984; Stöffler et al., 1985*). The Descartes Formation is mostly ejecta from the older Nectaris Basin. The overlying Cayley Formation, emplaced by the younger Imbrian(?) impact event, consists mostly of reworked material from the Descartes Formation with some Imbrian ejecta. Both the Descartes and Cayley Formations are inferred to rest on an older (pre-Nectaris) megaregolith composed of a thick layer of complex debris from many older impact events. Numbers refer to specific collected samples that are representative of the various units inferred to be present. LM shows where the Lunar Module landed.

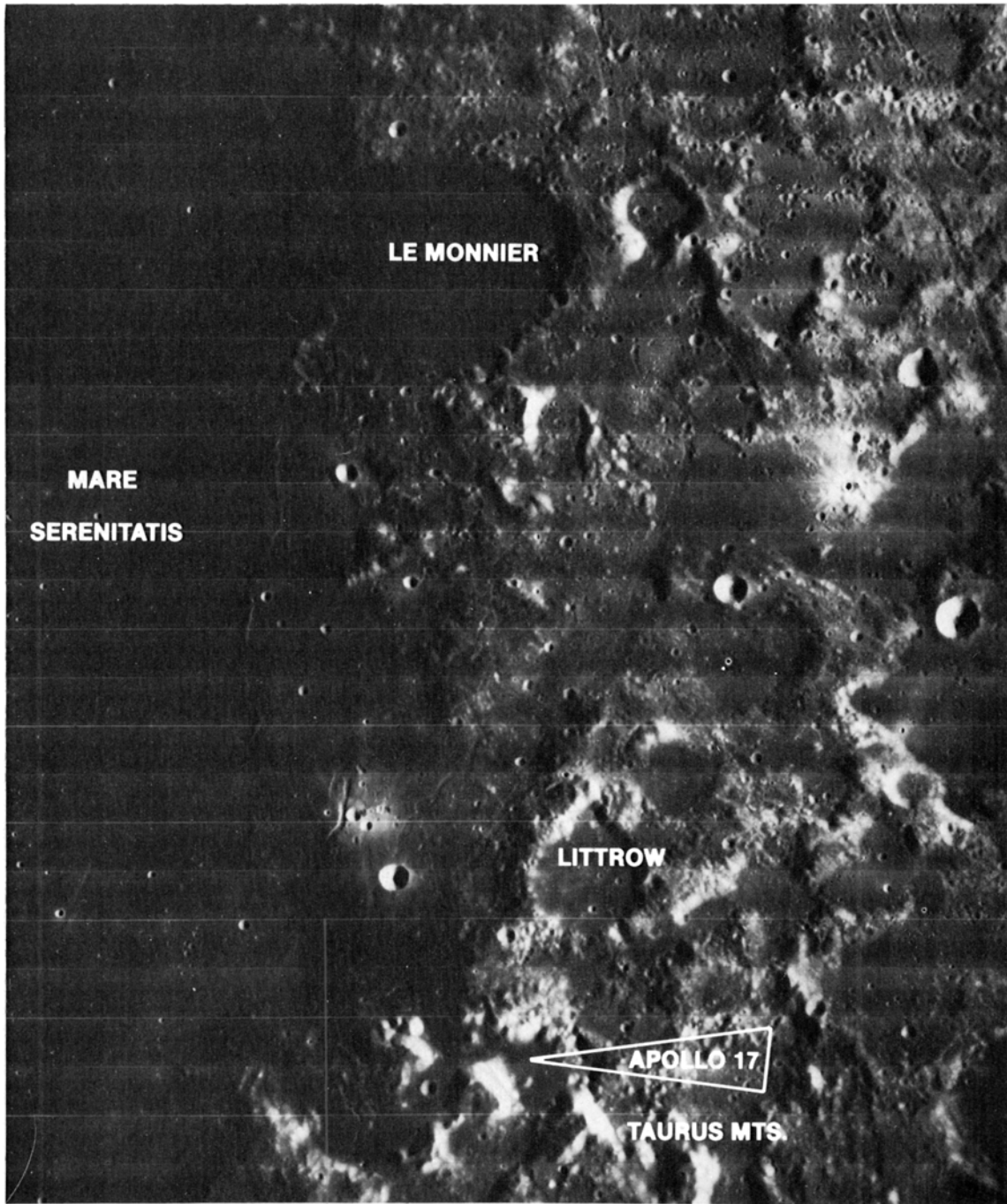


Fig. 10.26. Regional view of the Taurus-Littrow region on the eastern rim of Mare Serenitatis, showing the Apollo 17 landing site. Lunar north is at top. The Taurus Mountains (light-colored highland material at right) form the actual rim of the mare. These massifs are embayed by the later basalt lava flows (darker material at left) of Mare Serenitatis itself. The unusually dark color of the material around the actual landing site (bottom center) is due to the presence of dark-mantle deposits (glass-rich pyroclastic units). Horizontal lines are framelet boundaries in this Lunar Orbiter photograph. Each framelet is 12 km wide. (NASA Photo LOIV-78H3.)

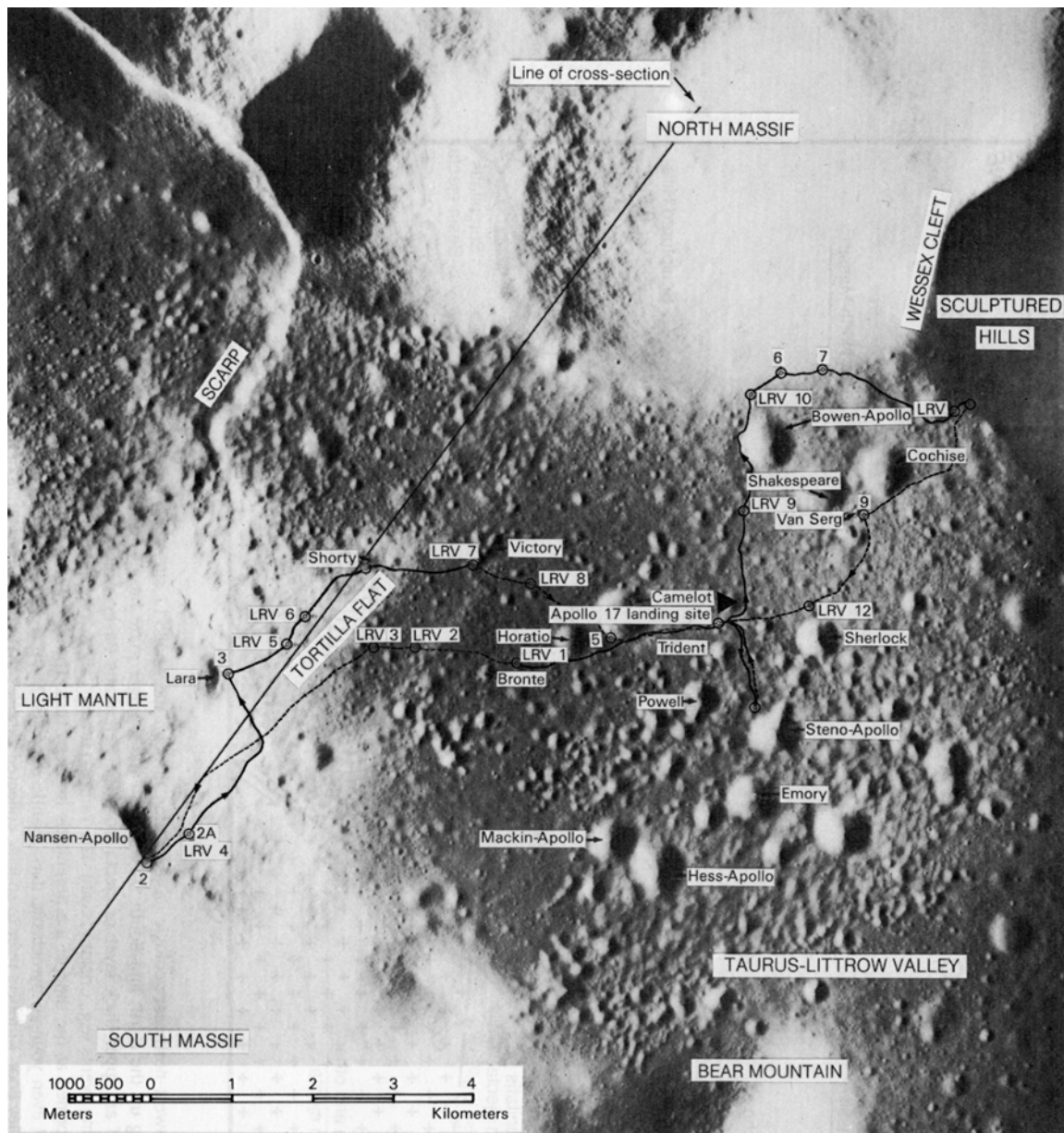


Fig. 10.27. Apollo 17 site traverse map, showing topographic features, informally-named craters, scientific sites, and astronaut traverses. Solid lines are used where the traverse is known, dashed lines where the traverse is approximate. The LM landing site (center flag) is in an east-west-trending valley (Taurus-Littrow Valley) that is floored by basalt lavas and bounded by two high massifs of older highland material (North Massif, South Massif). During traverses with the Lunar Roving Vehicle (marked LRV, with numbered stops), the astronauts studied and sampled both the basalts on the valley floor and the highland material from the massifs. Numbered stations not preceded by "LRV" are formal sampling stations, as opposed to informal samplings made at points of interest during the LRV traverses. (Defense Mapping Agency Chart 43D1S2 (25); original scale 1:25,000.)

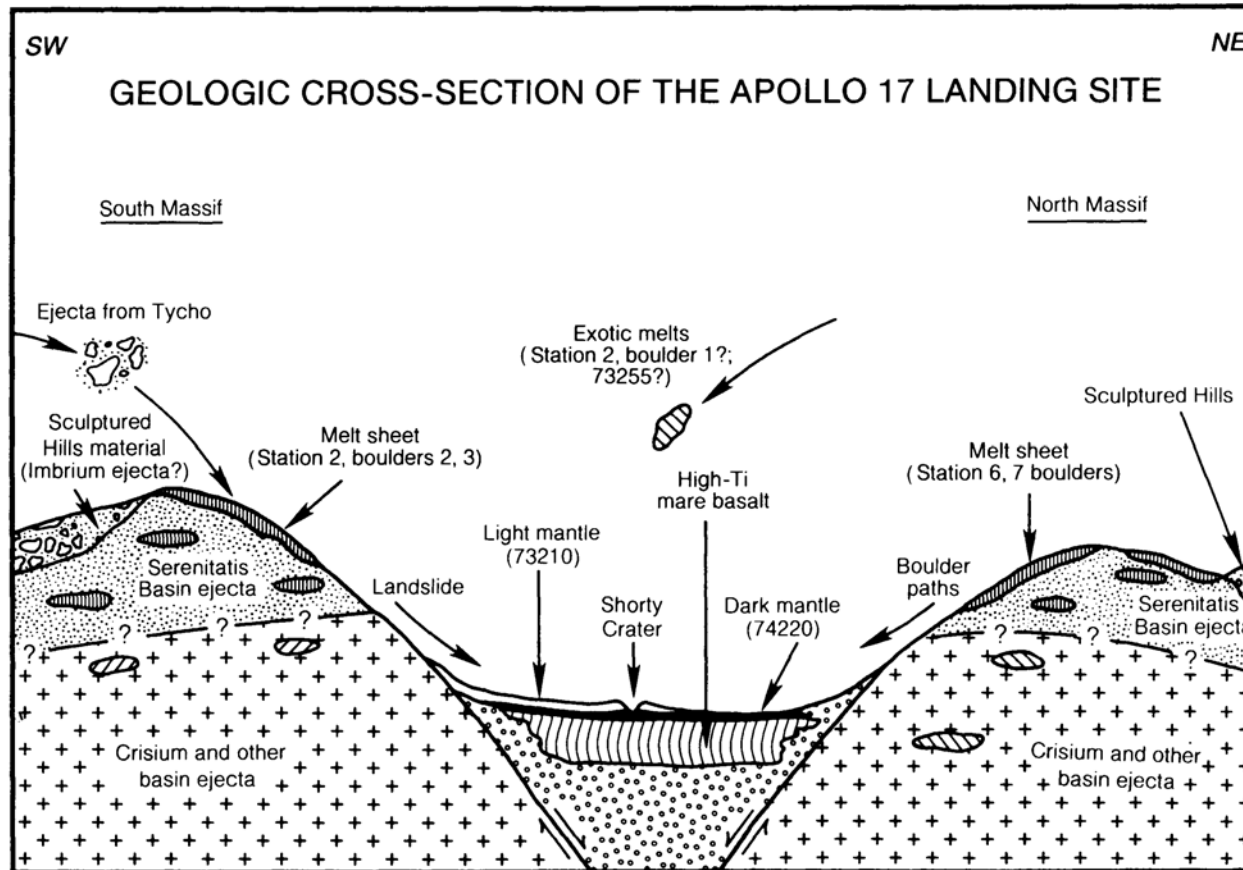


Fig. 10.28. Schematic southwest-northeast geologic cross-section through the Apollo 17 site, showing the complex boundaries between older highland material (ejecta layers making up the North and South Massifs) and the younger mare basalt flows that underlie the valley (modified after Wolfe *et al.*, 1981). The massifs consist of an upper thick layer of ejecta from the Serenitatis Basin, which is inferred to overlie an even thicker layer of complex ejecta from earlier basin-forming events (e.g., Crisium Basin). The Taurus-Littrow Valley developed as a downdropped wedge (graben) between two fractures (faults) that may have been formed at the time of the Serenitatis impact event. The valley was then filled, first with fragmental debris from the massifs, then by basalt lava flows and even younger pyroclastic dark-mantle deposits. More recent geological activity includes landslides and boulder falls from the higher massifs onto the valley floor. Numbers refer to specific collected samples that are representative of the various units inferred to be present.

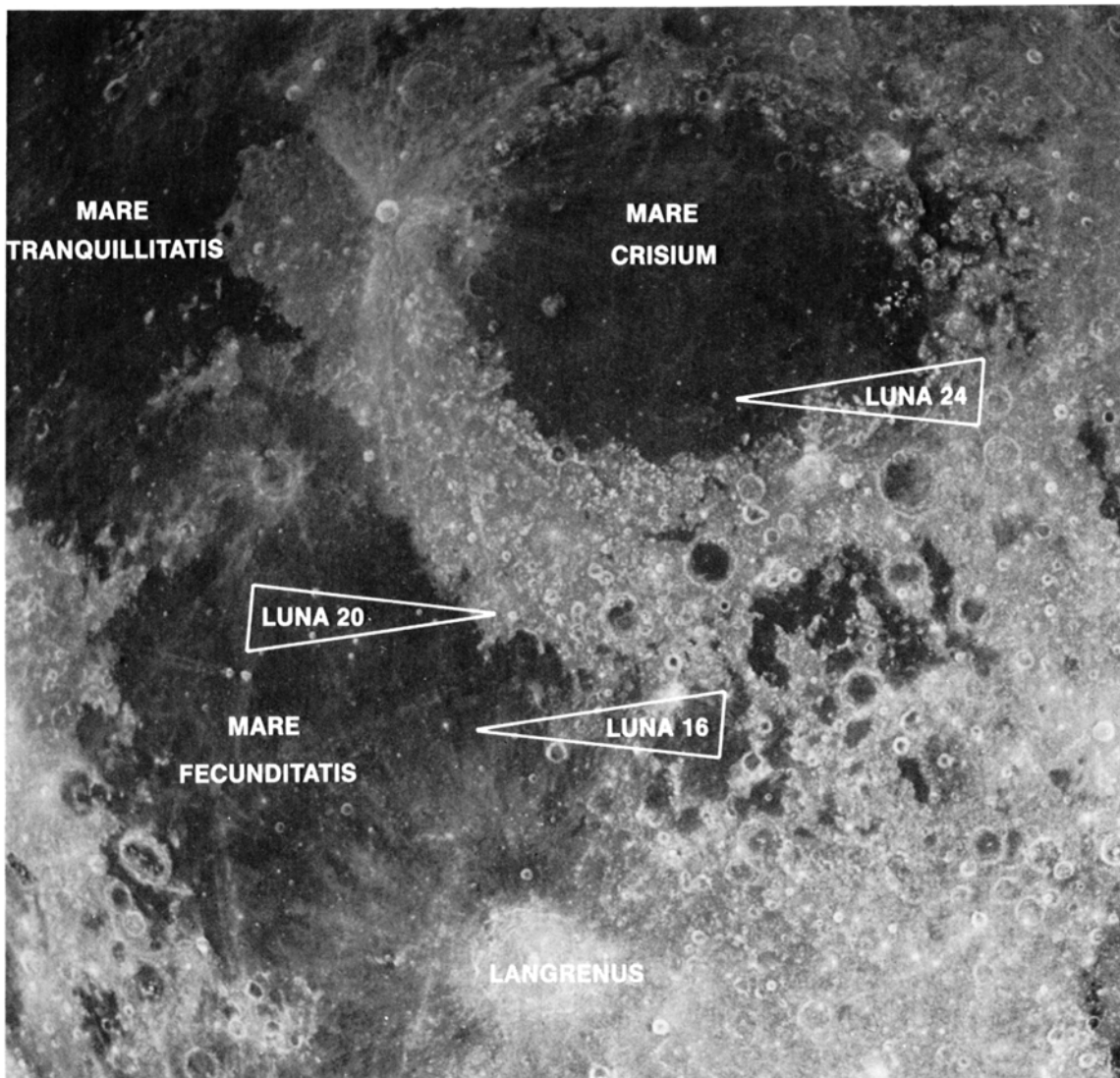


Fig. 10.29. Regional view of the east limb of the Moon, showing landing sites for the U.S.S.R. Luna 16, 20, and 24 robotic sample-return missions. Lunar north is at top; approximate width of view is 1200 km. Luna 16 and 24 sampled mare basalt lavas from Mare Fecunditatis and Mare Crisium, respectively. Luna 20 returned a sample of highland material from the outer edge of the ejecta deposits surrounding Mare Crisium. (Portion of NASA Photo AS11-44-6661.)

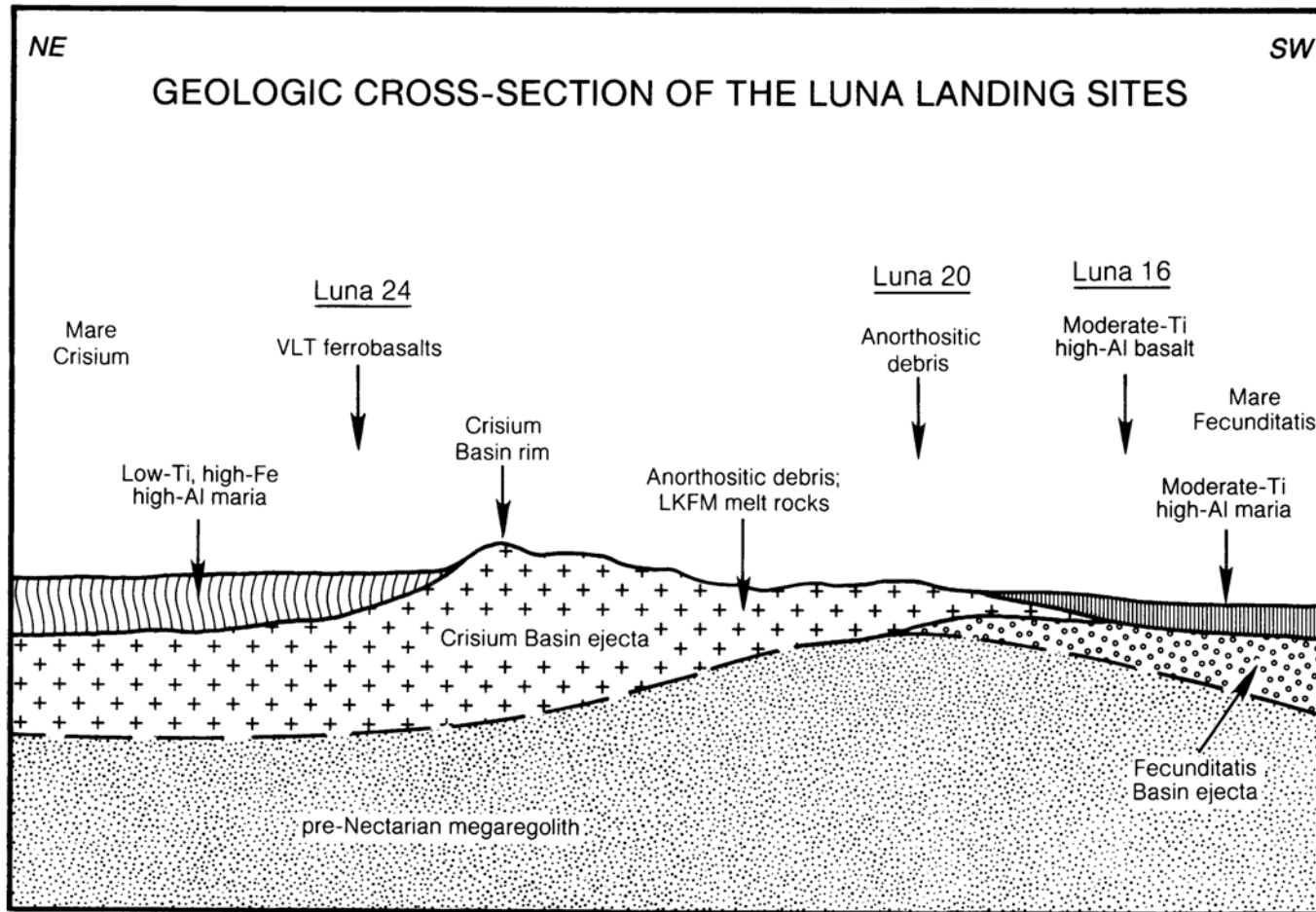


Fig. 10.30. Schematic north-south geologic cross-section through the region of the Luna 16, 20, and 24 landing sites (modified after *Wilhelms*, 1984). The highland regions, whose geology has been inferred from regional relations, consist of layers of complex ejecta deposits from large impact basins, Fecunditatis (older) and Crisium (younger). These units in turn rest on a thick layer of megaregolith consisting of ejecta from even older (pre-Nectarian) impact basins and craters. All ejecta layers were probably deposited before 4.0 b.y. ago and some were subsequently covered by a variety of lava flows. Note that the lavas covering Mare Crisium (left) are significantly different chemically from the flows on Mare Fecunditatis (right).

ultramafic composition and pyroclastic origin. The Apollo 15 site is one of the most geologically complex areas visited by any Apollo mission (Fig. 10.22), and remains the subject of active research. Discussions of the site geology may be found in *Swann et al.* (1972) and *Spudis and Ryder* (1985, 1986).

10.6.5. Apollo 16

The Apollo 16 mission was sent to the central lunar highlands near Descartes Crater (landing site: 9°S, 15.5°E; Fig. 10.23). The main mission objective was to sample two morphologic units representative of highland geology, the relatively smooth Cayley Plains and the hilly and furrowed Descartes material, both of which were suggested prior to the mission to be of volcanic origin. A secondary objective was to examine the lunar highlands at a point distant from any mare. Three long EVAs were performed using the LRV (Fig. 10.24), sampling and examining these two geologic units as well as two recent impact craters 1–2 km in diameter.

In sharp contrast to premission expectations, the returned samples are all impact products, mostly polymict breccias and impact melts (see section 6.4) with some pristine anorthositic rocks (see section 6.3). The extensive Apollo 16 sample suite shows clearly that neither the Cayley nor Descartes unit is volcanic in origin. Current interpretations of these units involve origins as impact-ejecta deposits, somehow related to the formation of the Imbrium and Nectaris Basins, although the exact contribution of each basin to the deposits at the Apollo 16 site is unknown. It is possible to interpret some absolute ages of impact melt rocks from the Apollo 16 site as the time of formation of the Nectaris Basin (3.92 b.y.). One of many possible interpretive cross-sections through the Apollo 16 site is shown in Fig. 10.25. The geology of the Apollo 16 site is discussed in detail by *Ulrich et al.* (1981), *James and Hörz* (1981), *James* (1981), *Spudis* (1984), and *Stöffler et al.* (1985).

10.6.6. Apollo 17

The last Apollo mission was sent to a highland/mare boundary near the southeastern rim of the Serenitatis Basin, the Taurus-Littrow Valley (landing site: 20.2°N, 30.8°E; Fig. 10.26). Planning for this site was probably the best of any Apollo mission, thanks to previous experience and the extensive orbital data obtained from the Apollo 15 mission. Objectives included the examination of two massifs (highlands), where rocks from deep in the lunar crust might be found (as Serenitatis and other basin ejecta), study of the valley subfloor, which was presumed to

consist of mare basalts, and examination of a low-albedo deposit that discontinuously mantles both highlands and mare at the site. Three long traverses were completed with the LRV (Fig. 10.27), and the premission objectives were spectacularly accomplished.

The subfloor of the valley does indeed consist of high-Ti mare basalts, of which several chemical subgroups can be distinguished; they range in age from about 3.8 to 3.7 b.y. The highland massifs bounding the valley consist of complex impact-melt breccias and plutonic igneous rocks of the Mg-suite (see section 6.3.4). The impact-melt breccias show an assembly age of 3.87 b.y. This value may reflect the age of the Serenitatis Basin, but it is uncertain how many cratering or basin-forming events were involved in the origins of these samples. A dark-mantle deposit on the valley floor consists of orange and black pyroclastic fragments, with a high-Ti basaltic composition, about 3.64 b.y. old. A light-mantle unit at the site is an avalanche deposit from the South Massif, apparently initiated by the impact of ejecta from Tycho Crater, about 2000 km away. Cosmic-ray exposure-age measurements of the light mantle material indicate that it was exposed about 100 m.y. ago, and may be interpreted as evidence that both the landslide and the formation of Tycho occurred at that time. The geologic reconstruction of the Apollo 17 site is given in Fig. 10.28; discussions of the geology of the Taurus-Littrow region may be found in *Schmitt* (1973), *Wolfe et al.* (1981), and *Spudis and Ryder* (1981).

10.6.7. The Luna Landing Sites

Between 1970 and 1976, the U.S.S.R. sent three unmanned sample return missions to the Moon, all of which landed (apparently for operational reasons) on the eastern limb of the lunar nearside. Each spacecraft was designed to drill a shallow core into the regolith, remove the core, and return it to Earth. The geology of the specific sites cannot be deciphered directly because of the lack of other data; therefore, this discussion concentrates on the regional geology of the lunar eastern limb.

The Luna 16 mission landed in northern Mare Fecunditatis (landing site: 0.7°S, 56.3°E) in September 1970, Luna 20 landed in the highlands south of the Crisium Basin (landing site: 3.5°N, 56.5°E) in February 1972, and Luna 24 landed in southern Mare Crisium (landing site: 12.7°N, 62.2°E) in August 1976 (Fig. 10.29).

The Luna missions provided us with samples from two different mare deposits and one highland region; the latter site is probably dominated by ejecta from the Crisium Basin. The Luna 16 mission returned

material from a mare basalt regolith; fragments consist of a moderately-high-Ti, high-Al variety of basalt. One "large" basalt fragment (<0.1 g) was successfully age-dated, giving a formation age of 3.41 b.y. Luna 20 returned a small sample from a highland (anorthositic) regolith; most lithic fragments consist of granulites, anorthosites, impact melts, and polymict breccia fragments. The most successful mission in the Luna series, Luna 24, returned a 1.6-m-long core of mare regolith from Mare Crisium. Basalt fragments in the sample are very low in Ti

and high in Fe and Al; measured ages on these basalts range from 3.6 to 3.4 b.y. A regional cross-section showing the general geology of the Luna sites is shown in Fig. 10.30. More detailed discussions of the local and regional geology of these sites are found in the following references: Luna 16, *McCauley and Scott* (1972); Luna 20, *Heiken and McEwen* (1972); Luna 24, *Head et al.* (1978); see also *Wilhelms* (1984) for a discussion of the regional stratigraphy of all three sites.